TURUN
YLIOPISTO
UNIVERSITY
OF TURKU

OPTIMIZING MRI-GUIDED PROSTATE ULTRASOUND ABLATION THERAPY USING RETROSPECTIVE ANALYSES AND ARTIFICIAL INGELLIGENCE

Cameron Wright

TURUN YLIOPISTON JULKAISUJA – ANNALES UNIVERSITATIS TURKUENSIS
SARJA – SER. D OSA – TOM. 1693 | MEDICA – ODONTOLOGICA | TURKU 2023

TURUN
YLIOPISTO
UNIVERSITY
OF TURKU

OPTIMIZING MRI-GUIDED PROSTATE ULTRASOUND ABLATION THERAPY USING RETROSPECTIVE ANALYSES AND ARTIFICIAL INGELLIGENCE

Cameron Wright

TURUN YLIOPISTON JULKAISUJA – ANNALES UNIVERSITATIS TURKUENSIS
SARJA – SER. D OSA – TOM. 1693 | MEDICA – ODONTOLOGICA | TURKU 2023

University of Turku

Faculty of Medicine
Radiology
Doctoral Programme in Clinical Research
Department of Radiology, Turku University Hospital

Supervised by

Professor, Roberto Blanco Sequeiros
Radiology
University of Turku
Turku, Finland

Professor, Peter J Boström
Urology
University of Turku
Turku, Finland

Reviewed by

Professor, Jochen Walz
Department of Urology
Institut Paoli-Calmettes Cancer Centre
Marseille, France

Professor, Heikki Nieminen
Department of Biomedical Engineering
Aalto University
Helsinki, Finland

Opponent

Professor, Jurgen Fütterer
Department of Imaging
Radboud University Medical Center
Nijmegen, Netherlands

The originality of this publication has been checked in accordance with the University of Turku quality assurance system using the Turnitin OriginalityCheck service.

ISBN 978-951-29-9182-2 (PRINT)
ISBN 978-951-29-9183-9 (PDF)
ISSN 0355-9483 (Print)
ISSN 2343-3213 (Online)
Painosalama, Turku, Finland 2023

Edina and Noah

UNIVERSITY OF TURKU
Faculty of Medicine
Department of Clinical Medicine
Radiology
CAMERON WRIGHT: Optimizing MRI-guided prostate ultrasound ablation therapy using retrospective analyses and artificial intelligence
Doctoral Dissertation, 114 pp.
Doctoral Programme in Clinical Research
February 2023

ABSTRACT

Magnetic resonance imaging (MRI)-guided transurethral ultrasound ablation (TULSA) is an emerging therapy that has been used to treat prostate cancer (PCa). TULSA destroys prostate tissue with heat using therapeutic ultrasound. The heating is monitored in real-time using MRI thermometry. Despite TULSA's promise, there are several challenges that have slowed its widespread adoption. Fortunately, MRI images and heating parameters from all TULSA treatments are stor ed. By conducting detailed retrospective analyses and applying deep learning on existing treatments, we can extract valuable information and then leverage this knowledge to optimize future TULSA treatments.

One major challenge occurs for those patients who had PCa radiation therapy failure and are seeking salvage treatment with TULSA. Many of these patients have leftover metal markers in the prostate. These markers can hamper subsequent TULSA therapy because they introduce susceptibility artifacts in the MRI image and may also block the ultrasound, which may compromise treatment safety and efficacy. Through an extensive retrospective analysis, we have determined that gold markers tend not to affect the treatment outcome, except when located simultaneously close to the urethra and far from the target boundary, or when located directly on the target boundary itself. Clinically, gold markers had no apparent effect on treatment safety and efficacy compared to a control cohort without markers at the 12-month follow-up. Conversely, nitinol markers are generally problematic for TULSA.

A second major challenge applies to all TULSA treatment indications. Immediately after TULSA therapy, MRI contrast agents are used to visualize the non-perfused volume, an objective measure of the ablation outcome. Unfortunately, even if undertreatment is observed, retreatment is not possible, forcing an additional treatment several months later, and with it the associated risks of a second intervention. By training a deep learning model with existing TULSA treatment-day, contrast-free MRI image sets, we have predicted the non-perfused volume with an accuracy comparable to modern-day deep learning prostate segmentation methods.

Overall, this work will help daily clinical practice and increase the odds of a successful TULSA therapy.

KEYWORDS: prostate cancer, fiducial markers, deep learning, artificial intelligence, MRI thermometry, thermal ablation, contrast-enhanced MRI

TURUN YLIOPISTO
Lääketieteellinen tiedekunta
Kliininen laitos
Radiologia
CAMERON WRIGHT: MRI-ohjatun eturauhasen ultraääniablaatiohoidon optimointi retrospektiivisten analyysien ja tekoälyn avulla
Väitöskirja, 114 s.
Turun kliininen tohtoriohjelma
Helmikuu 2023

TIIVISTELMÄ

Magneettikuvaus(MRI)-ohjattu virtsaputken kautta annettu ultraääniablaatio (TULSA) on uusi primaarin ja sädehoidon jälkeen paikallisesti uusiutuneen eturauhassyövän (PCa) hoitomuoto. Menetelmässä eturauhaskudosta koaguloidaan korkean intensiteetin ultraäänellä reaaliaikaisessa MRI-ohjauksessa, mikä parantaa hoidon tarkkuutta. Lupaavista kliinisistä tuloksista huolimatta MRI-ohjaus altistaa teknisille ja kliinisille haasteille, mitkä ovat hidastaneet TULSA-hoidon laajempaa käyttöönottoa. TULSA-hoidossa jokainen vaihe rekisteröidään MRI-kuvin. Koneoppimista hyödyntämällä voidaan retrospektiivisesti analysoida näitä MRI-kuvia TULSA-hoitotulosten optimoimiseksi.

Sädehoidon ohjauksessa käytetyt eturauhaseen asetetut merkkijyvät saattavat vaikuttaa TULSA-hoidon tehoon ja turvallisuuteen uusiutuneessa PCa:ssä, koska ne voivat aiheuttaa artefaktoja MRI-kuvaan ja estää ultraäänen etenemisen. Laajassa retrospektiivisessa analyysissä todettiin, että kultamerkkijyvät eivät yleensä vaikuta hoitotulokseen, elleivät ne sijaitse samanaikaisesti lähellä virtsaputkea ja kaukana hoitokohteesta tai suoraan kohteen edessä. Kultamerkkijyvillä ei ollut ilmeistä vaikutusta hoidon turvallisuuteen ja tehokkuuteen verrattuna kontrolliryhmään ilman merkkijyviä 12 kuukauden seurannassa.

Välittömästi TULSA-hoidon jälkeen hoitotulos varmistetaan merkkiainetehosteisilla MRI-kuvilla, joilla visualisoidaan verenkierroton alue, mikä korreloi akuuttiin kudosvaurioon eli onnistuneeseen hoitovasteeseen. Ongelmana on, että vaikka merkkiainetehosteisissa MRI-kuvissa todettaisiin riittämätön hoitovaste, uudelleenhoito ei ole samalla hoitokerralla mahdollista, koska eturauhaseen kerääntynyt merkkiaine estää hoidon. Tällöin tarvitaan uusi hoitokerta kuukausien kuluttua toimenpiteen sisältämineen riskeineen, mikä viivästyttää hoitoa ja kuormittaa potilasta. Tässä tutkimuksessa onnistuttiin tarkasti ennustamaan verenkierroton alue hoidonaikaisista merkkiainetehostamattomista MRI-kuvista hyödyntämällä syväoppimismallia.

Näillä havainnoilla on tärkeä kliininen merkitys TULSA-hoitotulosten parantamisessa.

AVAINSANAT: eturauhassyöpä, merkkijyvät, syväoppiminen, tekoäly, MRI-ohjaus, ultraääniablaatio, merkkiainetehosteinen MRI

Table of Contents

Abbreviations

AE	Adverse event
AS	Active surveillance
AX	Axial
CE	Contrast-enhanced
CEM43	Cumulative equivalent minutes at 43°C
CT	Computed tomography
DSC	Dice similarity coefficient
EBRT	External beam radiation therapy
ECD	Endorectal cooling device
EPI	Echo planar imaging
EPIC-26	Expanded prostate cancer index composite
GBCA	Gadolinium-based contrast agents
HIFU	High intensity focused ultrasound
IIEF-5	International index of erectile function
IPSS	International prostate symptom score
ISUP	International society of urological pathology
MAE	Mean absolute error
MAG	Magnitude
MSE	Mean squared error
MRI	Magnetic resonance imaging
NVB	Neurovascular bundle
PCa	Prostate cancer
PET	Positron emission tomography
PRFS	Proton resonant frequency shift
PSA	Prostate specific antigen
PSMA	Prostate specific membrane antigen
PSNR	Peak signal-to-noise ratio
QoL	Quality of life
RF	Radiofrequency
RP	Radical prostatectomy
SAG	Sagittal

SSIM	Structural similarity index
sTULSA	Salvage MRI-guided transurethral ultrasound therapy
SUB	Subtraction contrast image
T	Tesla
T1w	T1-weighted
T2w	T2-weighted
TDose	Thermal dose
TE	Echo time
TMax	Maximum temperature
TR	Repetition time
TULSA	MRI-guided transurethral ultrasound ablation
UA	Ultrasound applicator

List of Original Publications

This dissertation is based on the following original publications, which are referred to in the text by their Roman numerals:

I Wright C, Mäkelä P, Anttinen M, Sainio T, Boström PJ, Blanco Sequeiros R. Fiducial markers and their impact on ablation outcome for patients treated with MR-guided transurethral ablation (TULSA): a retrospective technical analysis. *International Journal of Hyperthermia*, 2021; 38(1): 1677-1684.

II Mäkelä P, Wright C, Anttinen M, Boström PJ, Blanco Sequeiros R. Safety and efficacy of MRI-guided transurethral ultrasound ablation for radiorecurrent prostate cancer in the presence of gold fiducial markers. *Acta Radiologica*, 2022; 0(0).

III Wright C, Mäkelä P, Anttinen M, Boström PJ, Blanco Sequeiros R. Deep learning prediction of non-perfused volume without contrast agents during prostate ablation therapy. *Biomedical Engineering Letters*, 2022; 0(0).

1 Introduction

Prostate cancer (PCa) is the second most common cancer and a leading cause of cancer deaths for men (Culp et al., 2020; Mottet et al., 2022). If the cancer develops to a point where it is deemed clinically significant, local treatment is recommended (Mottet et al., 2022; NCCN, 2022).

Conventional first-line therapeutic options for PCa include radical prostatectomy (RP) and external beam radiation therapy (EBRT) (Mottet et al., 2022; NCCN, 2022). These therapies have concentrated historically on eradicating the disease, but potentially at the expense of the patient's quality-of-life (QoL) (Resnick et al., 2013; Sanda et al., 2008). Considering the favorable prognosis after PCa diagnosis, patients must live with these side effects, often for the remainder of their lives.

Despite their focus on disease eradication, recurrence may still occur after conventional therapy. For example, up half of all patients may undergo biochemical recurrence at some point in their lifetimes after EBRT (Cornford et al., 2017; Mottet et al., 2022). Non-curative, systemic androgen deprivation therapy (ADT) for radiorecurrent PCa is the standard treatment option, but also carries debilitating long-term side effects (Tran et al., 2014).

To overcome the limitations of conventional therapies, a variety of alternative local treatment options have emerged in both the primary and salvage PCa setting, including laser ablation, cryoablation and high-intensity focused ultrasound (HIFU) ablation. These minimally invasive procedures have strived to offer comparable disease control, but with an improved safety profile. One of the newer and promising alternatives is magnetic resonance imaging (MRI)-guided transurethral ultrasound ablation (TULSA), which has been utilized for different indications with encouraging outcomes (Anttinen et al., 2020; Klotz et al., 2020; Lumiani et al., 2021).

Several factors differentiate the TULSA technology from other minimally invasive procedures. TULSA thermally coagulates the prostate "inside-out" by delivering high-intensity, spatially-directed ultrasound via a transurethral catheter. The heating source originates at the prostatic urethra and radiates outwards towards the prostate capsule. This provides inherent protection to the surrounding anatomy, in particular the rectum. MRI imaging is used to both plan and monitor the treatment

in real-time, a benefit which is leveraged to increase both the safety and efficacy of the treatment. Finally, conformal ablation is fully automated through the use of a closed-loop treatment controller, an effective technique to mitigate both over- and undertreatment.

Nevertheless, despite these technological benefits, TULSA has many inherent challenges that can negatively affect treatment outcomes. In the context of radiorecurrent PCa, many patients have leftover fiducial markers. Theoretically, several fiducial marker properties could accumulate and result in poor safety and efficacy. For example, local susceptibility artifacts emanating from the markers could contaminate the MRI images, to such an extent that they obscure large parts of the anatomy (Mougenot & Moonen, 2017; Schenck, 1996). Another reason is that markers could block the ultrasound heating, leading to undertreatment behind the marker and with it the risk of undertreating the lesion (Bakaric et al., 2018; Georgiou et al., 2017; Suomi et al., 2018). Lastly, the ultrasound heating which does not penetrate beyond the marker could instead deposit directly in front of the marker, leading to local hotspots and increasing the safety risk, particularly near the urethra (Bakaric et al., 2018). There is a pressing need to understand the consequences of undergoing TULSA for the treatment of radiorecurrent PCa for those patients harboring fiducial markers.

Real-time thermometry monitoring of TULSA, regardless of the treatment indication, also continues to be challenging. While thermometry is a powerful monitoring technique, it is a relative measurement technique, not absolute. It is sensitive to patient motion and air artifacts (Winter et al., 2016). To confirm the extent of ablation after treatment completion, gadolinium-based contrast agents (GBCA) are injected immediately post-treatment, and the non-perfused volume is measured on the contrast-enhanced (CE) MRI-image (Staruch et al., 2017). If undertreatment is suspected, the physician has no means to re-treat, due to specific GBCA properties (Hijnen, Elevelt, & Grüll, 2013; Hijnen, Elevelt, Pikkemaat, et al., 2013). A second TULSA procedure is feasible, but must be rescheduled, increasing costs, patient stress (de Sousa et al., 2012), and re-introducing the risks of a second general anesthesia procedure. Physicians therefore need additional tools to help ensure that the prostate was fully ablated during the first treatment to avoid the consequences of undertreatment.

Fortunately, we are well-positioned to tackle these challenges, due to the wealth of existing imaging, safety monitoring and biopsy data acquired before, during and after TULSA. A thorough review of these prior treatments and patient characteristics can reveal trends, insights, and guiding principles to optimize future treatments.

Based on a comprehensive review and analysis of prior treatments, the first objective of this doctoral thesis was to assess both the technical implications and clinical safety and efficacy for patients who underwent TULSA treatment harboring

residual fiducial markers. These results should culminate in practical treatment planning guidelines for future patient treatments. The second objective was to establish the feasibility of an artificial intelligence (AI) model capable of predicting the immediate non-perfused volume based on contrast-free, treatment-day TULSA MRI imaging sequences. This was achieved by utilizing imaging databases already available from existing TULSA therapies.

2 Review of the Literature

2.1 Prostate anatomy and function

The prostate is a “walnut-sized” organ found deep in the male pelvis which has two main functions: its primary function is reproductive, responsible for components of seminal fluid that support male sperm. The second function relates to urinary control.

The prostate is surrounded by critical anatomy (Figure 1), located directly inferior to the bladder, anterior to the rectum, and posterior to the pubis bone. The prostate gland is supported by pelvic floor muscles, including the levator ani and obturator. At both ends of the prostate, two small muscles at the urethra entry (bladder sphincter) and exit (urethral sphincter) surround the prostatic urethra The urethral sphincter in particular plays a key role in urinary continence. Seminal vesicles, which store seminal fluid and sit just outside the prostate, merge with the ductus deferens coming from the testes into ejaculatory ducts. These ejaculatory ducts penetrate the prostate until they reach the prostatic urethra.

Various physiological systems interact with the prostate. First, the prostatic urethra provides a passage for urine to exit the body. Second, blood supply to the prostate is provided via the internal iliac artery, which then branches into the inferior vesical, middle rectal, and internal pudendal arteries. Blood drainage occurs via the prostate venous plexus, traveling onwards to the internal iliac vein. Third, the prostate is innervated with sympathetic and parasympathetic nerve fibers. The small vessels and nerve fibers intertwine at the neurovascular bundle (NVB) and surround the prostate. Located at the posterolateral corners, the NVB has been described as a complicated network of finely dispersed nerves and blood vessels (Takenaka et al., 2005). Finally, lymphatic drainage of the prostate occurs via the external iliac, internal iliac, sacral, and common iliac lymph nodes.

The prostate itself can be divided into zones, including the central, transitional, peripheral zones in addition to an anterior fibromuscular stroma layer (McNeal, 1981). The peripheral zone accounts for roughly 70% of the prostate and is the only region that can be palpated during a digital rectal exam (McNeal, 1981). The prostate gland itself is a mixture of glandular and fibromuscular tissue. A pseudo-capsule encapsulates the prostate gland, with the inner layer composed of connective tissue and the outer layer composed of fascia.

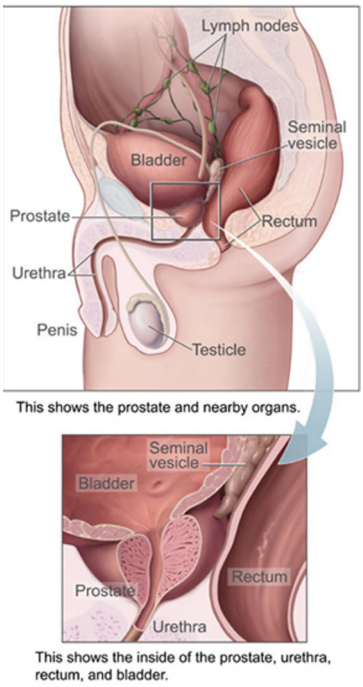

Figure 1. Prostate and surrounding anatomy (Courtesy of National Cancer Institute)

2.2 Prostate cancer

The majority of PCa begins with the uncontrolled growth of prostate cells (adenocarcinomas). Within the prostate itself, over two thirds of PCa lesions originate in the peripheral zone, while the others originate in the transitional zone (Epstein et al., 1994; McNeal et al., 1988). While some patients are diagnosed with unilateral disease, most PCa tends to be multifocal (Wise et al., 2002). Multifocal lesions may have different tumor sizes and grades. The lesion with the higher grade or volume is referred to as the index lesion. Scientific evidence indicates that the index lesion is the strongest predictor of disease progression (Ahmed et al., 2012; Algaba & Montironi, 2010; Arora et al., 2004; Karavitakis et al., 2011; Wise et al., 2002). PCa can extend to surrounding organs or spread via the lymphatic or blood systems.

Unlike other cancers in the body, the prognosis of PCa is favorable, due to its comparatively slow progression and low clinical burden. Patients diagnosed with PCa at a later life may never develop symptoms until their death (Mottet et al., 2022). Nevertheless, while many patients are diagnosed with low-risk disease with low metastatic potential, PCa can also manifest as intermediate- and high-risk disease, and these tumors can lead to PCa-related mortality.

Epidemiology and risk factors

PCa is the second most diagnosed cancer in males (Culp et al., 2020). In 2020, it was estimated that there were 1.4 million PCa diagnoses worldwide (IARC, 2022). The likelihood of having PCa at an early age is low, but steadily increases with age. At ages greater than 79 years, the prevalence of PCa is 59% (Bell et al., 2015). PCa is a global phenomenon, but depending on testing methods and geographical location, rates of diagnosis are highly variable. The incidence and disease stage are related to biological, genetic and lifestyle factors. Death from PCa is comparable across the globe, except for men of African descent with slightly worse odds (Mottet et al., 2022).

Various risk factors for PCa have been researched including environmental factors, diet, weight, among many others, but often lack the quality data needed to draw firm correlations. For this reason, according to the European guidelines, no effective preventative steps can be recommended at this time (Mottet et al., 2022) to lower the risk of a PCa diagnosis.

Classification and staging

PCa classification is a function of how pervasive the tumor is within the prostate, whether the tumor has extended beyond the prostate capsule or to regional lymph nodes, and if any distant metastases are present. Current European guidelines utilize the Tumour, Node, Metastasis (TNM) classification system (Brierley et al., 2017). Higher values for T, N and M are indicative of more advanced disease. N and M assessment is done via imaging. Clinical T-stage classification has been routinely assessed via digital rectal exam, but radiological T-stage classification is becoming more prevalent. European guidelines also utilize the European risk group classification (Cooperberg et al., 2005), which reflects the risk of biochemical recurrence after conventional therapy like surgery or radiation therapy.

Histological tumor grading

If deemed suspicious, biopsy specimens from the prostate and surrounding anatomy are taken to establish the tumor grade. The Gleason score is a histopathological assessment from 1-5 of the tumor architecture (Gleason, 1966). It is used to rank the most extensive primary tumor pattern present in the prostate, plus the second most common pattern (Mottet et al., 2022). As tumors evolve, their gland formation gets increasingly disordered and chaotic, and glands are given progressively higher scores. In 2014, the International Society of Urological Pathology (ISUP) endorsed a modified version of the original Gleason grading system which limited

pathological grading to be capped from 1-5 which considers the tumor grading from both the primary and secondary lesions.

The ISUP Gleason Grade Group (GG) score, along with the clinical TNM stage and the prostate specific antigen (PSA) measurement, constitute the European risk group assessment. Table 1 summarizes the different PCa risk groups (A.V. et al., 1998).

Table 1. European risk group classification for prostate cancer (Modified from Mottet et al. 2022)

Low-risk	Intermediate-risk	High-risk	
PSA < 10 ng/mL and ISUP GG 1 and cT1-2a	PSA 10-20 ng/mL or ISUP GG 2/3 or cT2b	PSA > 20 ng/mL or ISUP GG 4/5 or cT2c	any PSA any ISUP GG cT3-4 or cN+
Localized			**Locally advanced**

2.2.1 Diagnosis

PCa is often suspected from either an elevated PSA measurement or abnormal digital rectal exam finding. If this is the case, the disease is definitively diagnosed with confirmation from imaging and a histopathological specimen acquired from prostate biopsy. However, the disease may also be incidentally confirmed after unrelated prostate surgery, such as for the treatment of benign prostatic hyperplasia (BPH). In today's clinical practice, physicians use a combination of PSA, biopsies, and imaging to confirm and grade PCa.

PSA

PSA is a serum marker which is organ-specific but importantly not PCa-specific. For this reason, other prostate conditions can also cause elevated PSA, including BPH and prostatitis. Despite these limitations, PSA has revolutionized PCa diagnosis due to its simplicity and low cost (Stamey et al., 1987), and when considered as an independent variable, has been shown to be a strong predictor of PCa (Catalona et al., 1994). Nevertheless, due to its lack of specificity, other diagnosis methods are still needed for proper diagnosis.

Imaging

In the last decade, MRI has firmly entrenched itself as the imaging modality of choice for diagnosis of PCa. This is due to its comparatively high contrast and resolution, ability to map tumor perfusion and diffusion, among others. Moreover,

the clinical community has made enormous strides towards PCa MRI reading standardization, used for the detection and grading of lesions. These standards have gone through several iterations including the Likert score (Dickinson et al., 2011) and later the Prostate Imaging Reporting and Data System (PI-RADS, v2.1) (Turkbey et al., 2019). MRI has demonstrated good sensitivity for local PCa detection, particularly for those tumors with ISUP GG ≥ 2 (Borofsky et al., 2018; Bratan et al., 2013; Johnson et al., 2019), but less so for ISUP GG 1 (Bratan et al., 2013). Perhaps counterintuitively, MRI's lack of ISUP GG 1 sensitivity may be a positive for both patients and healthcare systems. This is because ISUP GG 1 is considered indolent low-risk disease and treatment of this disease type is questionable. By only highlighting clinically significant disease, MRI can help prevent overdiagnosis and unnecessary prostate biopsies. In modern clinical practice, a PI-RADS score ≥ 3 is often used as a benchmark before prostate biopsy is administered. Nevertheless, despite its utility, MRI is still vulnerable to intra- and inter-operator variability and is currently not established enough to entirely obviate the need for histopathological confirmation of the disease. Figure 2 is an example that highlights the sensitivity of multiparametric MRI for lesion detection.

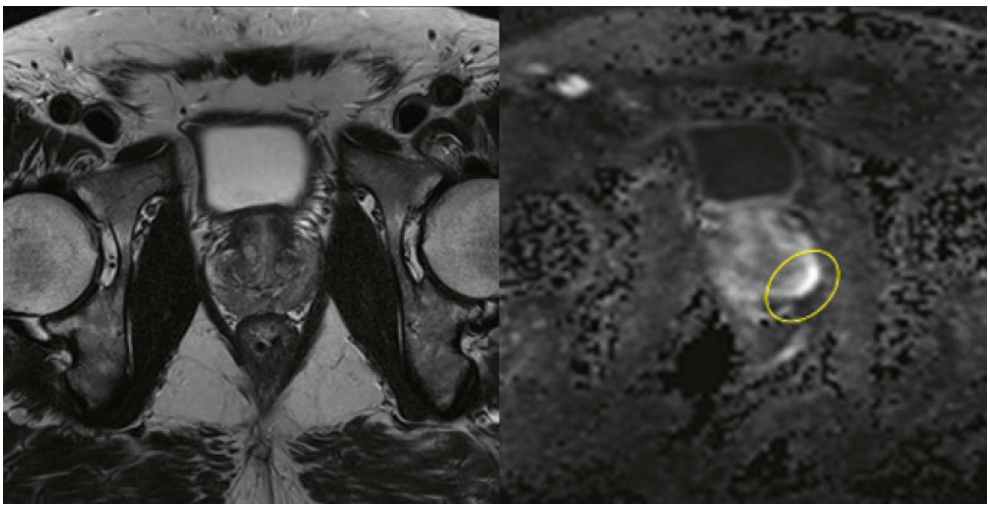

Figure 2. Multiparametric MRI. The left image, despite higher resolution and contrast, does not show obvious signs of disease. The same prostate is imaged with a scan sensitive to diffusion, revealing the presence of a PI-RADS 4 lesion on the left posterolateral corner (Bomers et al., 2020).

N-staging is typically performed with either computed tomography (CT) or abdomen/pelvic MRI, which have sensitivities near 40% (Harisinghani et al., 2003; Hövels et al., 2008). More recently, prostate specific membrane antigen (PSMA) positron emission tomography (PET) has been investigated for N-staging. PSMA is

an enzymatic trans-membrane protein located on the cell membrane, and it has been found that virtually all primary PCa tumors and metastases express this enzyme (Silver et al., 1997; Sweat et al., 1998). Reported sensitivity and specificity values for ^{68}Ga-PSMA PET of 77% and 97% (Perera et al., 2020), the most widely used PSMA-tracer, have been reported. PSMA-PET/CT is the currently the most effective N-staging modality, but due to its comparatively low spatial resolution, smaller lymph node metastases may still be missed (Mottet et al., 2022). Widespread adoption is still dependent on more clinical data.

For M-staging, bone scintigraphy has been the most common imaging modality for detection of bone metastases, with sensitivity and specificity rates of 79% and 82% (Shen et al., 2014). More recently, whole-body MRI and PSMA-PET/CT have been increasingly utilized (Mottet et al., 2022), with encouraging outcomes. There is still a need for more clinical evidence available to fully endorse MRI and PSMA-PET/CT as the N- and M-staging gold standards, but as this field of imaging develops, this may quickly change (Mottet et al., 2022).

Biopsy

Histopathological evidence of the PCa is the most definitive proof of tumor presence and grade currently available to clinicians. If deemed appropriate, the physician may ask the patient to undergo a prostate biopsy to confirm the digital rectal exam abnormalities, PSA and imaging findings. Current European guidelines recommend that if the MRI is positive with a PI-RADS score ≥ 3, all prostate biopsies should be systematic plus targeted (Mottet et al., 2022).

Prostate biopsies may be administered using either the transrectal or transperineal approach, although the transperineal is preferred (Mottet et al., 2022). For systematic biopsies, a minimum of eight cores should be taken, and for larger prostates 10-12. If the physician elects for additional targeted biopsies, at least 3-5 cores should be taken from each suspicious MRI area.

2.2.2 Treatment

Conventional therapies

Depending on the TNM staging and tumor grading, several different treatment options may be offered to patients diagnosed with PCa. For the entirety of this doctoral thesis, only local treatment options will be examined. Conventional therapies have included active surveillance (AS), RP, and EBRT.

AS is a common option for many patients. The underlying principle of AS is as follows: for patients with both a long-life expectancy (> 10 years) and lower-risk

disease, the risks of mortality and clinical burden of PCa are low. Moreover, curative treatments such as RP and EBRT have non-negligible morbidities. Therefore, avoidance of unnecessary curative treatment is preferred, until such a time that the disease progresses beyond a defined threshold, at which point curative treatment may become more appropriate (Bruinsma et al., 2017). To track disease progression, patients are monitored closely, undergoing a regimented protocol of digital rectal examinations, PSA testing, MRI scans, and prostate biopsies. Overall, AS offers good long-term overall- (85%-100%) and cancer-specific survival (98%-100%) (Adamy et al., 2011; Carter et al., 2007; Khatami et al., 2007; Klotz et al., 2015; Roemeling et al., 2007; Soloway et al., 2010; Tosoian et al., 2015; van As et al., 2008). However, over one third of patients who initially opt for AS do eventually switch to curative treatment, due to a variety of factors including disease progression, disease volume, or patient preference (Mottet et al., 2022). As the disease progresses, the effectiveness of AS also decreases. Furthermore, the psychological burden of living with cancer is one of its pitfalls (Reeve et al., 2012; Taylor et al., 2018). Despite these limitations, AS has more recently gained prevalence as a treatment for intermediate-risk disease. This is driven primarily by the knowledge that in the absence of any active treatment, intermediate-risk disease still has overall good prognosis, with 10-year and 15-year PCa specific mortality rates of 13% and 20% (Walsh, 1997).

If a decision to undergo curative treatment has been made, conventional curative local treatment options RP and EBRT are typically offered. RP is a surgical option whereby the entire prostate and seminal vesicles are removed, which is commonly performed today either laparoscopically or with robotic assistance. Depending on disease characteristics and patient preferences, variations in the technique may be used, such as nerve sparing (Walsh & Mostwin, 1984; Walz et al., 2016), seminal vesicle sparing (Gilbert et al., 2017), among others. The efficacy of RP remains difficult to elucidate, particularly for lower-risk disease. On the one hand, one long-term randomized control study reported benefits of RP regarding overall and cancer-specific survival compared to watchful waiting (Bill-Axelson et al., 2018) after 29 years follow-up. On the other hand, other long-term large-scale randomized control trials have not (Hamdy et al., 2016; Neal et al., 2020; Wilt et al., 2017). The ProtecT trial also found lower rates of disease progression and metastases compared to AS at 10-years post-surgery (Hamdy et al., 2016; Neal et al., 2020). However, RP also carries a non-negligible morbidity. Urinary incontinence and erectile dysfunction are the most common side effects after surgery, with rates of 21% and 70% reported, respectively (Haglind et al., 2015; Mottet et al., 2022). Unplanned post-operative visits are also common, with emergency visit rates of 12% and hospital re-admission rates of 4% (Mukkala et al., 2021).

Many patients may also be offered EBRT as curative, non-invasive local treatment for PCa. EBRT uses ionizing radiation to destroy tissue. The combination of a beam collimator, rotational control, and detailed treatment plans are used to optimize the radiation dose delivered to the prostate and to spare the surrounding anatomy. To improve visualization of the prostate, fiducial markers are typically implanted in the prostate prior to the therapy, which persist indefinitely afterwards (O'Neill et al., 2016). Current EBRT options, including intensity-modulated, volumetric arc or image-guided RT, are the most effective approaches. It is now recommended that patients receive 74-80 Gray to reduce the likelihood of 5-year biochemical recurrence (Mottet et al., 2022). For intermediate- and high-risk disease, androgen deprivation therapy is also recommended in combination with EBRT for 4-6 months (Jones et al., 2011) and 2-3 years (Bolla et al., 2010), respectively. The risk of treatment-related toxicity after EBRT is also high, with urinary incontinence (3-9%), erectile dysfunction (61-94%) and bowel frequency/urgency/pain (16%) rates reported (Resnick et al., 2013).

Selecting one of AS, RP or EBRT is not straightforward, and is a function of the PCa risk group, life expectancy and patient preferences. This is compounded by the relatively low risk of dying from PCa. For example, patients with intermediate-risk disease who undergo non-curative treatment can expect a 10- and 15-year and prostate-cancer specific mortality of 13% and 20%, respectively (Walsh, 1997). For high-risk disease, the rates are 29% and 36%, respectively (Donohue et al., 2006). For patients with > 10-year life expectancy, current American guidelines recommend AS for low-risk, any therapy option for favorable intermediate-risk, and either RP or EBRT for unfavorable intermediate-risk and high-risk disease (NCCN, 2022).

Emerging ablative therapies

Due to the tradeoffs between efficacy and safety for conventional therapies, many researchers have explored alternative minimally-invasive curative treatment options for localized PCa. Minimally invasive approaches have typically used ablation to induce cell death. The theoretical advantages of ablation compared to surgery include better preservation of surrounding tissues, reduced hospitalization, lower morbidity, and high-resolution intra-procedural monitoring (Chu & Dupuy, 2014). Figure 3 is an illustration of which risk groups stand to gain the most benefit from ablative therapy compared to AS, RP, and EBRT.

Originally, minimally invasive techniques were used to treat the entire prostate gland. Both HIFU (Crouzet et al., 2014; Dickinson et al., 2016) and cryotherapy (Oishi et al., 2019) were explored, but due to long treatment times, prostate size limitations, or insufficient access to all regions of the gland, whole-gland ablation has become less common. However, these same therapies, as well as laser interstitial

thermotherapy, are also capable of performing partial ablation (L. et al., 2012; Shah et al., 2019; Valerio et al., 2017). The objective of partial ablation is to offer near-equivalent oncological control compared to conventional curative therapies, but with an improved safety profile by minimizing damage to non-diseased prostate tissue and important surrounding structures.

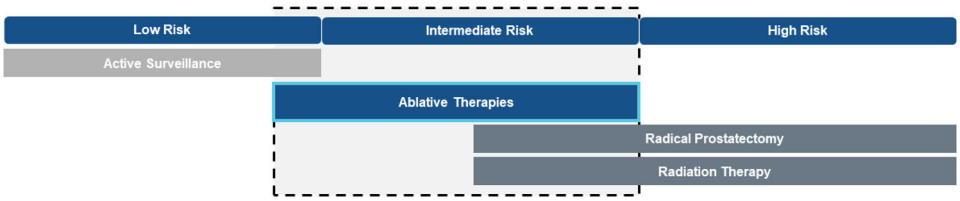

Figure 3. PCa risk groups who stand to gain most benefit by minimally invasive curative ablative therapies (Modified from Profound Medical Inc.)

Due to the lack of randomized control trials and relatively short follow-up, it is difficult to compare the efficacy of either whole-gland or partial ablation techniques to conventional therapeutic options. From a safety perspective, it is known that HIFU patients can expect rates of erectile dysfunction (23%), urinary incontinence (10%), rectal pain/bleeding (11%) and rectal-urethral fistula formation (0-5%) (Ramsay et al., 2015). For cryotherapy patients, they can expect the similar rates of 18%, 2-20%, 3% and 0-6% (Ramsay et al., 2015), respectively.

Salvage therapies

Recurrence after primary EBRT can also occur. Up to half of all patients treated with EBRT will undergo biochemical recurrence at some point in their lifetimes (Cornford et al., 2017). Noteworthy is that residual tumors tend to reappear where the index lesion was originally located (Cellini et al., 2002; Jalloh et al., 2015; Patel & Oto, 2016; Pucar et al., 2007). Irradiated prostates undergo significant structural changes in the years after therapy (Koopman et al., 2020), including size decreases and fibrosis (Coakley et al., 2003), obscuration of the zonal anatomy (Coakley et al., 2001), changes in the capsular patency (Koopman et al., 2020; Vargas et al., 2012) and decreased vascularity (Sugimura et al., 1990). The surrounding anatomy is also affected, with decreases in seminal vesicle size (Vargas et al., 2012) and the retropubic space occurring. These patients often have leftover fiducial markers (O'neill et al., 2016), which may obscure imaging and hamper future local treatments.

Even if the recurrence is believed to be local, 98% of patients will still receive non-curative systemic ADT, which has harmful long-term side effects (Tran et al.,

2014). Current alternatives include salvage prostatectomy (Chade et al., 2012), re-irradiation (Jereczek-Fossa et al., 2019), brachytherapy (Maenhout et al., 2018), HIFU (Crouzet et al., 2017) and cryoablation (Siddiqui et al., 2016), but all have drawbacks regarding toxicity and efficacy (Chade et al., 2012; Ingrosso et al., 2020).

MRI-guided transurethral ultrasound ablation

TULSA is a newer, minimally invasive MRI-guided intervention which uses high intensity ultrasound to thermally coagulate prostate tissue. While TULSA also thermally coagulates tissue, it does so "inside-out", with the energy emanating from the urethra outwards, instead of via the rectum or transperineally, which offers theoretical safety advantages for the rectum and surrounding tissues. TULSA has been used to treat several different prostate disease indications including whole-gland (Klotz et al., 2020), partial (Anttinen et al., 2019; Lumiani et al., 2021) and salvage PCa (Anttinen et al., 2020), as well as BPH (Viitala et al., 2021). The TULSA procedure is performed entirely in the MRI suite with the patient under general anesthesia and lying in the supine position.

Ablation is achieved via a transurethral catheter transducer (UA) which is inserted into the prostate shortly before the treatment begins. The catheter has ten individual elements (each element is 5 x 4.5 mm), which can be independently controlled for acoustic power and driving frequency. Each element can output up to four watts acoustic at low frequency operation and two watts acoustic at high frequency operation. TULSA transducers emit spatially directed but diffuse ultrasound, which allows the device to treat larger prostate volumes. In addition to the UA, an endorectal cooling device (ECD) is inserted into the rectum shortly before the ablation begins. Both the UA and ECD are connected to a water circuit, which continuously circulates room temperature water during the treatment, offering a protective cooling effect to both the prostatic urethra and the rectal wall.

A robotic arm secures the UA during the treatment for immobilization. The robotic arm is capable of both manual adjustments (height/tilt/linear) as well as automated finer precision motion control (linear/rotational).

An series of MRI treatment planning images are acquired after device insertion to first register the UA, adjust the linear position of the UA inside the prostate, and then finally help delineate the target volume. Once the physician has successfully demarcated the treatment zone, MRI thermometry is used to observe the ablation in real-time. MRI thermometry is a critical component of TULSA, because it allows the physician to observe the heat distribution in real-time, both inside the prostate but also to critical anatomy nearby. This includes: the pelvic floor muscles, the sphincter muscles, the rectal wall, the bladder neck, and the NVB.

The specific objective of the TULSA treatment is summarized below: all prostate tissue located two millimeters inside of the physician target boundary should achieve a temperature increase of 57°C. Figure 4 is a depiction of the TULSA treatment objective.

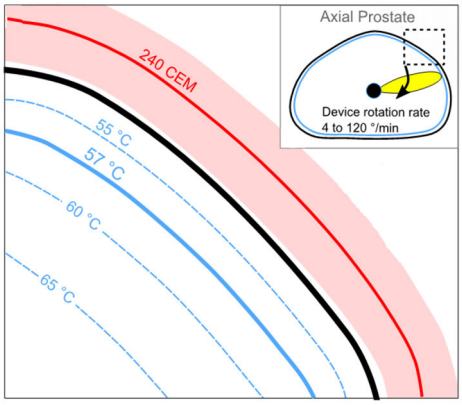

Figure 4. Objective of TULSA treatment. The entire prostate boundary is depicted in the small figure in the upper right square. The larger figure is a zoomed in view of a small segment of the prostate boundary. The black boundary (target boundary) is contoured by the physician during treatment planning. The objective is to ensure that all tissue two millimeters inside the target boundary reaches 57°C. The temperature gradients inside the prostate and the associated 240 cumulative equivalent minutes (CEM) are depicted for reference. (Courtesy of Profound Medical Inc.)

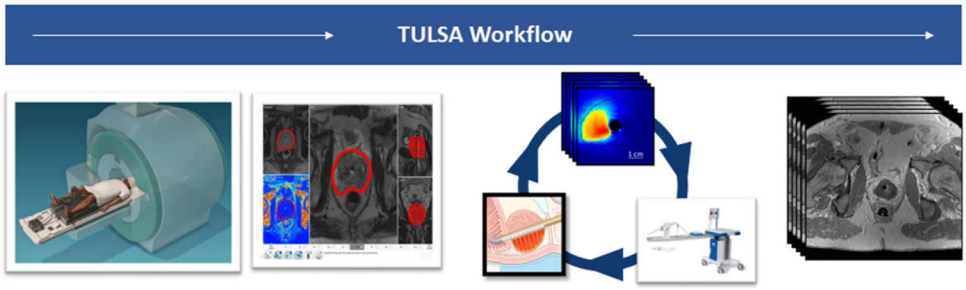

Figure 5. Description of TULSA workflow. UA and ECD are inserted into patient, and the patient is moved into the MRI bore. Imaging is used to localize the devices and plan the therapy. Once a plan is set, the ablation begins with thermometry temperature feedback. The controller monitors the temperature in real-time and adjusts power, frequency and rotation rotate to ensure conformal ablation. Contrast imaging is performed afterwards to monitor the non-perfused volume (From original publication III)

To satisfy this treatment objective, TULSA utilizes a closed-loop controller, which actively monitors the temperature distribution inside the target boundary. As new thermometry images arrive every six seconds spanning the entire prostate, the

controller measures the updated temperatures inside the target boundary and optimizes the ultrasound frequency, power, and rotational rate until the target volume has been completely ablated.

To confirm the extent of ablation, immediately after the therapy, GBCA are injected into bloodstream. The acute effects of the thermal ablation are determined by measuring the size of the non-perfused volume in relation to the contoured target boundary using a T1-weighted (T1w) CE-enhanced MRI sequence. An illustration of the TULSA workflow is shown in Figure 5.

2.2.3 Follow-up

Follow-up is a critical piece in the patient's management after PCa therapy. It is used to monitor both the oncological status after the intervention, and establish any treatment-related impact on safety and function. Follow-up protocols vary depending on the treatment received as well as on the clinical setting (primary vs. salvage). For conventional, first-line local curative treatments including RP and EBRT, current guidelines recommend PSA testing as the sole metric used to assess disease progression (Mottet et al., 2022), which typically occurs bi-annually up to three years after treatment, and then annually thereafter. For newer ablative therapies, disease monitoring is more rigorous and may involve PSA testing, MRI imaging and prostate biopsies. For patients with recurrent disease undergoing local salvage therapies, the same follow-up but with more extensive N- and M-staging is typical.

In addition to disease progression, treatment toxicity is also assessed. In the first months after therapy, any attributable adverse events (AE) are typically documented. Any changes in functional outcomes are also assessed. For clinical trials, physicians have attempted to quantify any loss in function through validated questionnaires which evaluate urinary incontinence, urinary bother/irritation, sexual/hormonal, and bowel function. Common validated questionnaires include the Expanded Prostate Cancer Index Composite (EPIC-26), International Prostate Symptom Score (IPSS) and International Index of Erectile Function (IIEF).

2.3 Ultrasound

Basic Principles

Ultrasound is a non-ionizing, mechanical wave which is capable of propagating through tissue and other physical materials. As an acoustic wave passes through a given medium, the individual particles in the wave's path displace about their resting position. Individual particles will first undergo compression, followed by rarefaction. During the compression phase, the material will experience positive

pressure, and during rarefaction phase, the pressure will be negative. Analogous to the electromagnetic spectrum, ultrasound constitutes the upper part of the sound spectrum: infrasound is defined as a frequency < 20 Hz, audible sound is from 20 Hz to 20 kHz, and ultrasound is > 20 kHz.

Ultrasound waves are characterized by several key parameters, including their driving frequency, pressure, intensity, and duration. Several factors dictate particle displacement, including various mechanical properties of the material and its temperature.

Acoustic Impedance, Attenuation, and Absorption

The ultrasound wave's mechanical energy loss is a function of several factors including scattering, absorption, refraction, and reflection. (Bamber, 2004). The physical medium in which the ultrasound wave originates and subsequently travels into plays a dominant role in determining the amount of energy loss due to reflections. Two physical properties of the material are particularly relevant: its density, and speed of the ultrasound wave as it travels through that particular medium. These values are unique to all materials such as water, bone, metal, and air. The acoustic impedance can be defined in the equation below for all materials:

$$\boldsymbol{Z = \rho * v} \tag{1}$$

where $\boldsymbol{Z}$ is the acoustic impedance in $kg \cdot s^{-1} \cdot m^2$, $\boldsymbol{\rho}$ is the tissue density in $kg \cdot m^{-3}$ and $\boldsymbol{v}$ is the speed of sound in the medium in $m \cdot s^{-1}$. Large differences in acoustic impedance will lead to large reflections. The fraction of reflected ultrasound energy between two surfaces is expressed using the following equation:

$$\boldsymbol{R = \left\{\frac{(Z_2 - Z_1)}{(Z_2 + Z_1)}\right\}^2} \tag{2}$$

where $\boldsymbol{R}$ is the fraction of reflected ultrasound energy, $\boldsymbol{Z_1}$ and $\boldsymbol{Z_2}$ the acoustic impedance of tissue 1 and 2. Table 2 highlights some representative acoustic impedances. It is readily apparent that as ultrasound travels from tissue into either air, bone, or gold, the vast majority will be reflected. For example, an ultrasound wave traveling from prostate tissue into gold will be ~90% reflected.

In addition to reflections, the ultrasound wave also undergoes energy loss as it propagates deeper into the same material. The amount of loss is a function of physical properties of the material itself, the ultrasound wave frequency, and the

length of the material. The attenuation coefficient α is expressed in units of dB · MHz^{-1} · cm^{-1}.

Table 2. Acoustic impedance of different materials

Material	Acoustic Impedance ($kg \cdot s^{-1} \cdot m^{-2}$)
Air	$0.0004 * 10^6$
Fat	$1.34 * 10^6$
Water	$1.48 * 10^6$
Muscle	$1.71 * 10^6$
Prostate	$1.66 * 10^6$
Bone	$7.81 * 10^6$
Gold	$62.53 * 10^6$

Table 3. Attenuation coefficients of different materials

Material	Attenuation Coefficient ($dB \cdot cm^{-1}$) at 3.5 MHz
Air	5.74
Fat	1.68
Water	0.0077
Muscle	3.915
Prostate	0.5-1.5
Bone	34.79
Iron	645*
Copper	208*
Nickel	318*

* performed at 5 MHz instead of 3.5 MHz

However, not all materials have an inverse relationship between attenuation and ultrasound frequency. For this reason, attenuation is often described in dB · cm^{-1} for specific driving frequencies. Table 3 below describes the attenuation coefficient for different materials at 3.5 MHz, a similar driving frequency to the TULSA device. There are significant attenuation differences in attenuation between air, water, prostate, muscle, bone, and metal.

Attenuation is comprised of two main components including absorption and scattering. The higher the driving frequency, the higher the resulting attenuation.

Energy that is absorbed by the tissue is converted to heat (Carstensen et al., 1990; Nyborg, 1988).

Ultrasound Generation

Ultrasound energy is commonly generated by electrically stimulating a piezoelectric crystal at its natural resonant frequency, causing it to vibrate mechanically at that same frequency. The pressure distribution directly impacts the spatial distribution of heating. Figure 6 shows the longitudinal heating pattern produced by the TULSA transducer.

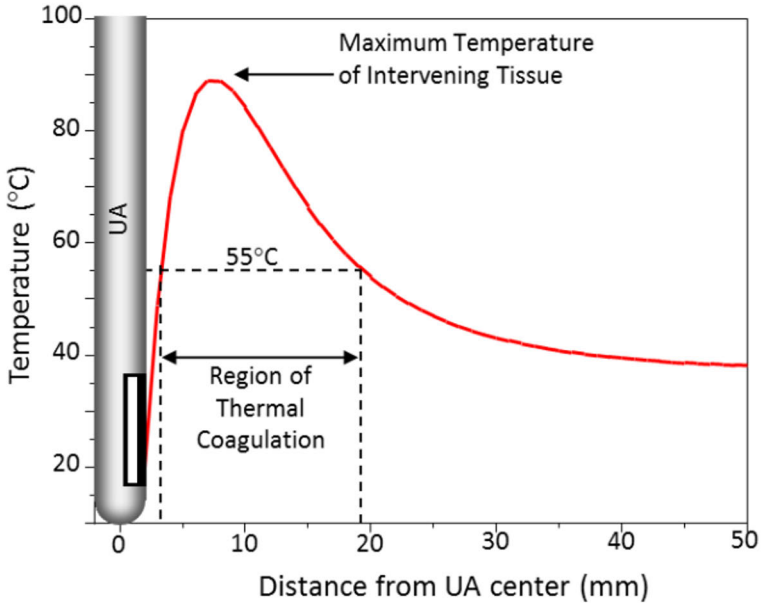

Figure 6. Spatial distribution of heating in the longitudinal direction produced by the TULSA device (Courtesy of Profound Medical Inc.)

The spatial distribution of acoustic pressure emanating from the source is variable and depends heavily on the piezoelectric geometry. For example, HIFU transducers are concave which allows to them to generate a high focal gain at some depth away from the transducer surface, but minimal amounts between the transducer surface and the focus. Conversely, the TULSA transducer is a 4.5x5mm rectangle, and its pressure profile in space is more diffuse.

2.3.1 Thermal ablation

Many newer, minimally invasive treatment modalities use thermal ablation to induce cell kill. Except for cryotherapy, therapies such as TULSA, HIFU and laser interstitial thermotherapy rapidly elevate the local tissue temperature. In a matter of seconds, modern ablative technologies can increase the local tissue temperature to 55°C, and in many cases above 80°C. Compared to conventional "slower" hyperthermia therapies, rapid ablative techniques can more easily overcome the heat sink effects resulting from blood perfusion (Mouratidis et al., 2019), which has the added benefit of shorter treatment times.

Ablation induces irreversible cell injury, leading to apoptosis and coagulative necrosis (Brace, 2011; Chu & Dupuy, 2014). In the prostate, after rapid exposure to elevated temperatures, the pattern of tissue damage has been classified into three distinct regions, including the coagulative necrosis zone, the apparently untreated zone, and a margin zone in between (Boyes et al., 2007). Cells in the coagulative necrosis zone are destroyed, with no coherent structure remaining. The untreated zone at the periphery is unaffected but can still show signs of edema and spontaneous cell necrosis. The margin in between is the most heterogenous, whereby tissues may retain their gland structures, but can undergo epithelium disorganization and may show signs of interspersed cell necrosis (Boyes et al., 2007). The size of the margin zone can be up to 5 mm (J. G. R. Bomers et al., 2017; Boyes et al., 2007; Chopra et al., 2012).

The likelihood of ablated tissue undergoing irreversible thermal injury is a function of both the local temperature and the exposure time. Sapareto & Dewey (Sapareto & Dewey, 1984) formulated the concept of thermal dose, an attempt to mathematically harmonize the likelihood of biological injury according to a reference temperature of 43°C, known as cumulative equivalent minutes (CEM43). It was found that the relationship was exponential, and for every 1°C increase in temperature, the amount of time halves to achieve the same toxic effect. The equation is described below:

$$\textbf{Thermal Dose} = \int_0^t \boldsymbol{R_{CEM}}^{(\mathbf{43}-\boldsymbol{T(t)})}\, \boldsymbol{dt} \qquad \textbf{(3)}$$

where $\boldsymbol{t}$ is the exposure duration in minutes, $\boldsymbol{T}$ is the achieved temperature in °C, and $\boldsymbol{R}$ is a constant whose value is 0.25 for temperatures < 43°C and 0.5 for temperatures > 43°C. To appreciate the exponential nature of thermal dose, Figure 7 shows the calculated thermal dose after 1s of exposure for temperatures ranging from 43°C to 60°C.

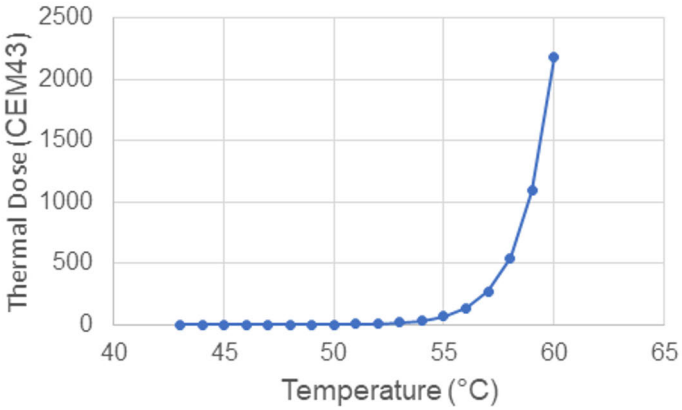

Figure 7. Calculated thermal dose for different temperatures thresholds after 1s of exposure to elevated temperatures.

Researchers have sought to identify which CEM43 thresholds are necessary to induce permanent cell damage. Depending on the tissue type, ranges between 30-250 CEM43 have been reported (C. A. Damianou et al., 1995; C. Damianou & Hynynen, 1994; N. J. McDannold et al., 2000; Venkatesan et al., 2012). For the prostate, *in vivo* evidence supports a value of 240 CEM43 (Hazle et al., 2002).

Despite this evidence, some researchers have questioned the reliability of 240 CEM43 threshold for rapid ablative therapies. The 240 CEM43 was developed for hyperthermia applications (40°C to 47°C) (Mouratidis et al., 2019) and may not apply to higher temperature thresholds. There is also conflicting *in vitro* evidence, where CEM43 thresholds of 150 000 were required to induce 99% necrosis of the sample (He et al., 2009). Establishing certainty is difficult due to the exponential dependency of temperature on thermal dose. To illustrate, for target temperatures of 55°C, 56°C and 57°C with a duration of 1s, the respective thermal dose would be 68, 136 and 273 CEM43, respectively, a factor of four increase with a temperature gradient of just 2°C. From a measurement perspective, achieving a 1°C accuracy with high temporal resolution is challenging.

Due to the inherent challenges with thermal dose, other researchers performing ablation in the prostate with TULSA have migrated to more binary outcomes for determining thermal coagulation. Specifically, they have used a temperature increase of 55°C as the necessary threshold to achieve acute thermal coagulation. These assessments are based on *in vivo* evidence with the TULSA device, which has indicated that 55°C corresponds to the region of acute coagulation on histology (Chopra et al., 2009). This region can grow over the weeks after therapy, in certain cases up to several additional millimeters (Anttinen et al., 2019; Burtnyk et al.,

2015). In the context of PCa and rapid ablation technologies, the thermal dose threshold requires more investigation.

2.4 Magnetic resonance imaging

Particularly in the last decade, MRI has firmly established itself as essential for both the PCa diagnosis and follow-up. Increasingly, MRI is also being utilized during image-guided therapies to both plan and monitor the treatment. The benefits of MRI are its soft-tissue contrast, high resolution in any spatial orientation, and lack of any ionizing radiation.

The signal measured during MRI acquisition is fundamentally determined by the hydrogen atom, which consists of a proton and an electron. Most biological tissues have roughly 70-90% water (H_2O) content, making it well-suited as a signal source (Brown RW et al., 2014; McRobbie et al., 2006; Weishaupt et al., 2006). In the absence of any external magnetic field, the proton spins, a fundamental property of protons, are randomly distributed in all directions, and their summation, expressed as the magnetization vector M_0, is null. However, when placed in an external static magnetic field B_0, slightly more proton spins align in the direction of B_0 compared to opposite it, creating a spatially dependent and non-zero M_0. These proton spins precess at a frequency determined by the Larmor frequency ω (Larmor, 1897). The precessional frequency is linearly proportional to B_0 and γ, the gyromagnetic ratio, a constant. However, even if one was equipped with a sensitive detector, a non-zero M_0 with precessing spins is still insufficient to record any signal.

To record signal, one must leverage the concept of nuclear magnetic resonance (NMR) (Rabi et al., 1938). When proton spins are excited with a radiofrequency (RF) pulse which is transmitted at the identical precessional frequency ω, the spins will absorb the RF energy, excite, and subsequently tilt their magnetization from the longitudinal direction (direction of static field) to the transverse plane, at which point it will precess about B_0. The RF pulse is known as the B_1 field, and the duration and power of the RF pulse determines what fraction of the longitudinal magnetization will tip into the transverse plane. Once the RF pulse is turned off, the magnetization will slowly recover to its preferred low-energy state, a state where the spins realign with B_0. The recovery process occurs via two separate mechanisms: spin-spin interactions relate to the decay of the transverse magnetization while spin-lattice interactions relate to the regrowth of the longitudinal relaxation. It has been found that both the decay and regrowth of the magnetization are exponential and can be described by time constants: T2 is the time constant that describes the decay in transverse magnetization and T1 is the time constant that describes the regrowth in the longitudinal direction. Transverse magnetization decay is a faster process than

longitudinal magnetization recovery. The equations below describe the magnetization dynamics in the transverse (xy) and longitudinal (z) directions:

$$S_{xy} = e^{-t/T2} \tag{4}$$

$$S_z = (1 - e^{-t/T1}) \tag{5}$$

Each tissue type has unique T1 and T2 relaxation time constants, typically on the order of milliseconds, which forms the basis of tissue contrast in MRI imaging, seen as regions of either dark, grey, or bright pixels on the image. The precessing magnetization in the transverse plane is detected with a receive coil. Figure 8 shows how different time constants can affect the magnetization dynamics.

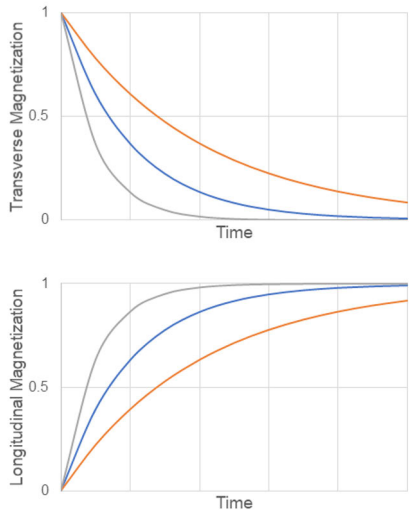

Figure 8. Effect of different T2 and T1 time constants on transverse and longitudinal magnetization. The smaller the time constant, the faster the transverse decay and the faster the longitudinal recovery.

The tissue-dependent nature of these recovery times after RF excitation and when the transverse magnetization is recorded forms of the basis of NMR contrast. The interval at which the proton spins are excited is referred to as the repetition time (TR). The time at which the signal is sampled is referred to the echo time (TE). The interplay between the TR and TE times impacts which type of tissue contrast is being measured, known as image weighting. In general, images may be T1w, T2-weighted (T2w) or weighted by proton density. For example, during T1w imaging, tissues with

short T1 times are brighter than those with long T1 times. For T2w imaging the effect is reversed.

To produce a T1w image, a short TR and TE is required. Conversely, to produce a T2w image, a long TR and TE is required. MRI sequences describe the interplay between TR, TE, and the flip angle. The most common sequences are spin echo and gradient echo (Elster, 1993). Spin echo sequences first excite the protons with a 90° RF pulse, and as the spin dephasing occurs, a second 180° refocusing pulse is applied, which leads to the formation of an echo. This refocusing has the added benefit that it reduces the effects of magnetic field inhomogeneities. Gradient echo sequences also use RF pulses, but then produce echoes using dephasing and rephasing gradients. The gradient dephasing and rephasing does not eliminate effects of magnetic field inhomogeneities, which explains why it is more sensitive. However, gradient echo sequences can be done more rapidly.

If we excite all tissue in the main magnetic field with the same B_1 pulse, we would not be able to spatially encode where in the tissue the signal originated from. For this reason, a third magnetic field is used, and is referred to as the spatially encoding gradients (Brown RW et al., 2014; McRobbie et al., 2006; Weishaupt et al., 2006). These gradients introduce a small, linear magnetic field which is slightly different than B_0 in the xy, and z planes. By modifying the frequency of the B_1 pulse we can achieve spatial encoding. The final sequence is a complicated interplay between B_0, B_1, TR, TE and the spatially encoding gradients.

2.4.1 Thermometry

MRI thermometry is an important aspect of ablative therapy as it allows physicians to non-invasively measure the temperature distribution inside the body in real-time. While many different approaches have been proposed, the most common is the proton resonance frequency shift (PRFS) technique (Ishihara et al., 1995). As tissues abundant with water molecules either heat up or cool down, the resulting temperature changes affect the hydrogen bonds, impacting the local magnetic field the nuclei experience, inducing a proton chemical shift (Mttixer & Reiter, 1965; Rieke & Pauly, 2008). Interestingly, the chemical shift change due to temperature changes is linear across a wide range of temperatures, varying by α, which has been experimentally determined to be -0.01 parts per million (ppm)/°C (Hlndman, 1966; N. McDannold, 2005; Rieke & Pauly, 2008). The temperature change is calculated by measuring the difference in phase between two images and is expressed below:

$$\Delta T = \frac{\emptyset - \emptyset_0}{\gamma \alpha B_0 TE} \quad (6)$$

where $\Delta \boldsymbol{T}$ is the temperature change in °C, $\emptyset_{\boldsymbol{0}}$ is the reference phase in radians, $\emptyset$ is the phase at the same location collected at some arbitrary time after the reference phase in radians, $\boldsymbol{\gamma}$ is the proton gyromagnetic ratio in radians·s^{-1}·T^{-1}, $\boldsymbol{B_0}$ is the main magnetic field in Tesla, and $\boldsymbol{TE}$ is the echo time in seconds (Rieke & Pauly, 2008).

Practically, to perform PRFS thermometry, a reference phase image is acquired prior to heating at every voxel location in the imaging volume. Once the ablation begins, the resulting temperature change is evaluated by measuring the change in phase at all voxel locations in the image. For this reason, PRFS thermometry does not generate absolute temperature measurements, and instead only calculates relative changes (Rieke & Pauly, 2008). The body's baseline temperature is typically measured shortly before the heating begins with an MRI-compatible temperature probe. To get as close to real-time monitoring as possible, thermometry is typically done with an echo-planar imaging (EPI) sequence (Stafford et al., 2004; Weidensteiner et al., 2003), which can acquire large scan volumes very rapidly. Based on the gradient echo imaging technique, the EPI sequence acquires multiple lines of k-space in a single RF excitation, using gradients to refocus the spins as it traverses through k-space. Figure 9 shows how thermometry can be used monitor the ablation in real-time.

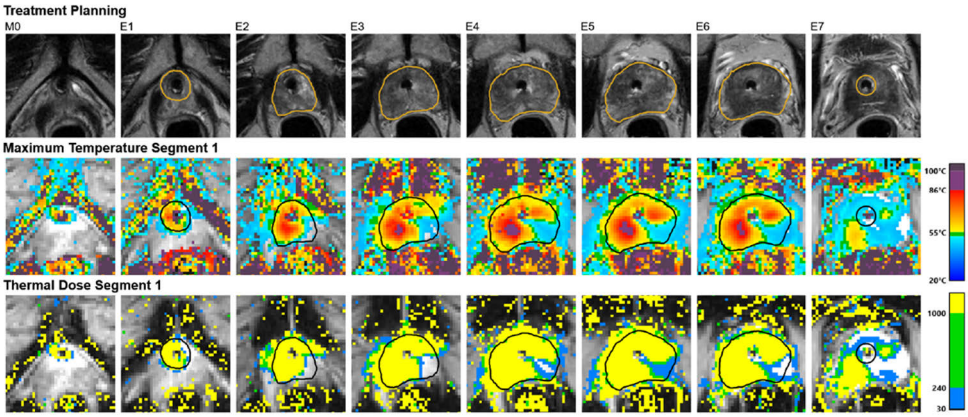

Figure 9. The physician leverages real-time thermometry to monitor the temperature distribution inside the body. Monitoring can be performed either by examining the maximum temperature increase in relation to the target boundary, or by examination of the thermal dose.

While thermometry is a powerful tool in the physician's arsenal, it has several limitations. First, due to its dependency on a reference image, it is inherently sensitive to patient motion, particularly interscan motion (Rieke & Pauly, 2008). Second, thermometry is also vulnerable to magnetic drift (Hijnen, Elevelt, Pikkemaat, et al., 2013), which may be relevant if the scan time is long. Third, while

it has been demonstrated that α is largely tissue-independent (Kuroda et al., 1998; Peters et al., 1998), that is not true for fatty tissue, which does not have the same hydrogen bonds as tissue comprised mostly of water. For this reason, fatty tissues have low α, making it challenging to measure temperature changes there. Partial volume effects may also occur if a voxel is comprised of both fatty and normal biological tissue (Odéen & Parker, 2019), and for this reason, fat suppression is commonly used during thermometry. Finally, thermometry is a reference-based temperature technique so errors in the baseline temperature can influence the outcome.

In addition to thermometry-specific limitations, thermometry may also exacerbate other well-established MRI artifact sources. One of the most prominent is the susceptibility artifact. Magnetic susceptibility is a feature of matter which characterizes how that material behaves when placed in a magnetic field. Susceptibility can be either diamagnetic or paramagnetic. Diamagnetic materials weaken the magnetic field, while paramagnetic materials strengthen it. Local regions of either strengthening or weakening of the magnetic field produce small local variations in B_0. Almost all biological tissues are weakly diamagnetic, while ferrous materials such as nickel and iron are highly paramagnetic. Gold is slightly diamagnetic, while the magnetic susceptibility of air is close to zero. Local susceptibility changes can cause two primary image artifacts including geometric distortion and overall signal loss. The local changes in the field disturb the linearity of the frequency encoding magnet, causing regional distortion (Arena et al., 1995; Taber et al., 1998). Moreover, these field inhomogeneities also lead to more rapid spin de-phasing because they modify the Larmor frequency of the material. This often leads to signal dropout (Shellock & Morisoli, 1994; Shellock & Shellock, 1996). Ferrous objects produce the most significant effects, but susceptibility differences between adjacent tissues, such as air interfaces, can also create these dropout zones. Since thermometry relies on EPI sequences, which uses gradient refocusing, these sequences are more vulnerable to susceptibility changes compared to spin-echo sequences (Port & Pomper, 2000). In the context of radiorecurrent PCa, susceptibility effects arising from fiducial markers can hinder the visualization of prostate tissue in the vicinity of fiducial markers (Jonsson et al., 2012; Maspero et al., 2018; Osman et al., 2019).

2.4.2 Contrast-enhanced imaging

Endogenous contrast differences are not always sufficient for highlighting specific pathologies or features of interest for the physician. Therefore, exogenous contrast agents are sometimes needed to enhance the signal intensity. There are numerous different MRI contrast agents on the market, but the most common are GBCA.

GBCA are injected into the veins and quickly perfuse to the rest of the body, followed by a rapid diffusion into the extracellular space (Mitchell, 1996), before eventually being filtered out by the kidneys. GBCA work in practice by shortening the T1 relaxation time of the hydrogen protons in their vicinity (Mitchell, 1996) and therefore are most effective when used in combination with T1w imaging.

CE-imaging has a key role in the context of ablative therapy monitoring, particularly when one considers the limitations of thermometry. Due to the decreased blood supply in the necrosed tissue, thermally coagulated regions of tissue become considerably more hypointense than the neighboring unexposed tissue (Knopp et al., 2001; Rivens et al., 2007). In addition to the hypointense core, known as the non-perfused volume, a hyperintense rim surrounds the necrotic core, a result of inflammation and hyperemia (Hectors et al., 2016). To emphasize differences in perfusion, the final CE-image is obtained by subtracting the native T1w image from the T1w image with contrast agent (N. J. McDannold et al., 1999; Rowland et al., 1997). Many researchers have demonstrated agreement between non-perfused volume and thermal dose (Hectors et al., 2016; Rowland et al., 1997). An example of CE-imaging after TULSA is shown in Figure 10.

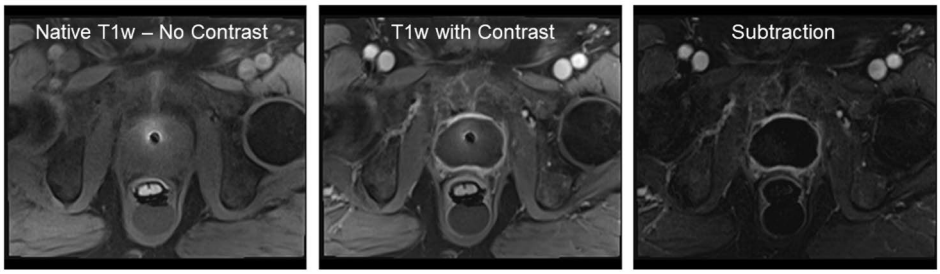

Figure 10. Example of CE-imaging after TULSA. The native T1w immediately after ablation does not discriminate either the non-perfused volume or the enhancing rim. The same sequence is repeated after the injection of GBCA into the veins. The CE-image highlights both effects. A subtraction of the two images further emphasizes these regions.

While CE-imaging can be beneficial to monitor response to therapy, it also has several drawbacks. First, GBCA are typically administered once at the very end of the procedure and never during thermometry acquisition. The predominant reasons are that the GBCA concentration in the body is dynamic after bolus injection and will decrease as a function of time. Additionally, GBCA can get trapped inside tissue under elevated temperature exposures (Hijnen, Elevelt, & Grüll, 2013). These two effects have several negative consequences. First, GBCA are paramagnetic and can cause field inhomogeneities thereby causing a local signal loss which make it difficult to extract signals where previous ablations took place, and which vary over

time. Second, GBCA can influence the PRFS equation, and introduce temperature errors anywhere from -4°C to +3°C (Hijnen, Elevelt, Pikkemaat, et al., 2013). Finally, it has been shown that the immediate non-perfused volume is not always the predictor of the final treatment outcome (Wijlemans et al., 2013). This is a result of the fact that the complete cell kill mechanisms can take many weeks after the therapy completion, possibly due to latent cell death from ischemia (Anttinen et al., 2019; Chu & Dupuy, 2014; Hectors et al., 2016). Despite the limitations, immediate non-perfused volume measurements are helpful for visualizing regions of undershoot or overshoot.

2.5 Artificial intelligence

The formal definition of AI was established in the 1950's by John McCarthy (McCorduck & Cfe, 2004), who stated that AI was "the science and engineering of making intelligent machines". A more concrete definition is that AI is a machine designed to solve problems that are typically reserved for humans, which is also capable of self-improvement. Particularly in the last decade, with the advent of faster computers and a global shift to digital infrastructure, AI has developed exponentially in the medical disciplines (Chan et al., 2020; Litjens et al., 2017). One remarkable attribute of AI that researchers have harnessed is its ability to interpret sensory information, which has led to numerous advances in applications including self-driving cars, language processing and computer vision (Hosny et al., 2018). AI is a highly diverse field of research, and various subspecialties have emerged under the AI umbrella.

2.5.1 Deep learning

Deep learning is a subset of machine learning, which itself is a subset of AI (Figure 11). Machine learning is defined as a machine's capacity to make informed predictions based on existing data, and as that data evolves, the machine can adapt to refine its predictions. The differentiation between deep learning and machine learning is which features of the existing dataset the machine model uses to make its prediction. In standard machine learning, it is the responsibility of the human to define these features. This requires an inherent understanding of which features are necessary, which may not always be possible. Deep learning, on the other hand, identifies its own features from the training dataset to generate a prediction without any human intervention required.

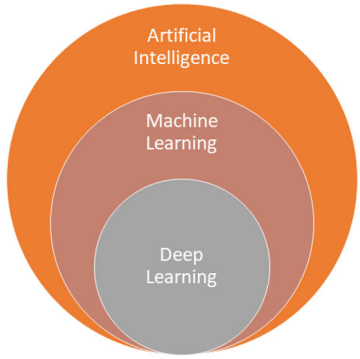

Figure 11. Relationship between artificial intelligence, machine learning and deep learning.

For radiology-based applications, deep learning models often employ supervised learning approaches. In its most basic form, this consists of a training dataset and labels. This is best illustrated with an example. Suppose a deep learning model is trying to predict cancerous lesions in the prostate based on screening MRI images. The training data is the screening MRI images, while the labeled data consists of radiologist-contours for each image. The deep learning model architecture is based on neural networks, illustrated in Figure 12. The model has an input layer (the inputs), an output layer (the prediction), and an indeterminate number of hidden layers. Hidden layers are used to synthesize the input data in various stages, typically from lower-level to higher-level features. At each new layer, a weight, bias, and non-linear activation function is used to process the inputs. A non-linear activation is necessary otherwise the model would be executing logistic regression.

For medical images, it is not practical nor meaningful to have each node connected to all other nodes during the stages of deep learning. For an input image with a height and width of 128x128 pixels, this would correspond to 16384 pixels. The number of nodes would exponentially increase with each layer making processing difficult. Perhaps more importantly, it is intuitive that the pixels on the upper left of the image share no relationship with the pixels on the bottom right of the image. To account for this complexity, it is customary practice to use convolutional neural networks (CNNs) to perform deep learning on medical images. CNNs have been around since the 1980's (Fukushima, 1980) but have increased in popularity in the last decade. At various stages of the learning process, the image is slowly synthesized into progressively higher-level features. Low-level features include features such as edges, lines, or dots, while high-level features could be the outlines of larger shapes. CNNs achieve this via a series of convolution and pooling processes. A desirable feature of CNN's is that they can accommodate multichannel data. An example CNN is illustrated in Figure 13.

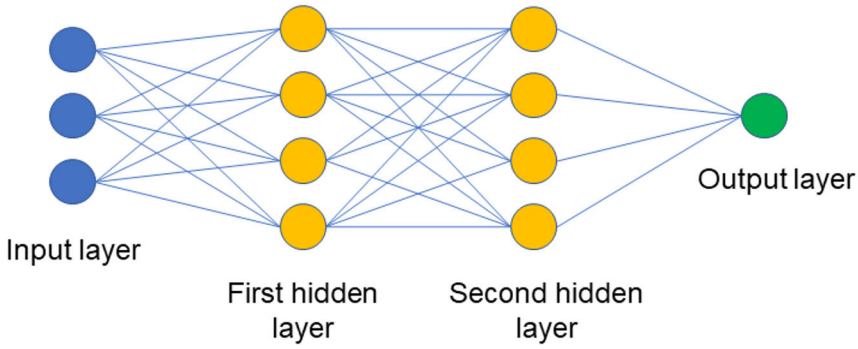

Figure 12. Concept of neural network with input layers, hidden layers, and output layers.

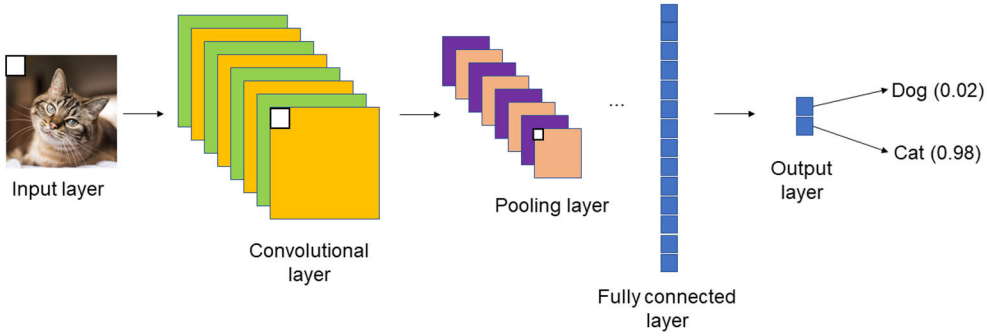

Figure 13. Illustration of CNN. An image of a cat is convolved with a 3x3 kernel to generate a new feature map. The process is repeated seven times with unique kernels, generating an image of the same pixel dimensions but with a depth of 8. Pooling is then performed to increase the signal-to-noise and simplify processing, which halves the image width and height. This process is repeated for as many times. Finally, the model makes a prediction if the image is a cat or dog with some associated probability.

The most common CNN for medical image segmentation and classification is the UNet model (Ronneberger et al., 2015). The name derives from the shape of the model and is illustrated in Figure 14. The UNet has been used to perform prostate segmentation (Aldoj et al., 2020; Cuocolo et al., 2021; Q. Zhu et al., 2017), prostate lesion identification (Schelb et al., 2019) and prediction of contrast uptake in the brain (Chen et al., 2021; Gong et al., 2018; Kleesiek et al., 2019). They have also been used to predict treatment outcomes (Abajian et al., 2018; Luo et al., 2020; Suomi et al., 2019). With the UNet model after a prediction is made, the model parameters are updated via back propagation, and the process is repeated to optimize the outcome.

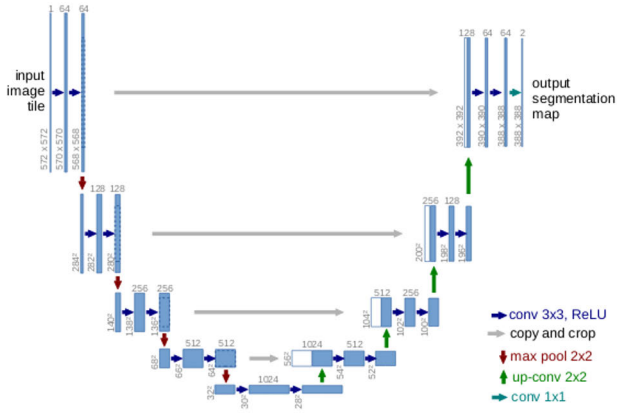

Fig. 1. U-net architecture (example for 32x32 pixels in the lowest resolution). Each blue box corresponds to a multi-channel feature map. The number of channels is denoted on top of the box. The x-y-size is provided at the lower left edge of the box. White boxes represent copied feature maps. The arrows denote the different operations.

Figure 14. Schematic of the UNet architecture, proposed by Ronneberger et al.

In practice, to validate a model's performance, the available dataset is separated into three groups: train, validation, and test. The train dataset is what the deep learning algorithm will use to identify correlations. The validation dataset is used iteratively during the training process to assess the generalizability of the model. The final model accuracy is measured on the test dataset, a dataset the model has never encountered, and is therefore the best representation of model generalizability. Roughly 70%-80% of the data is used for training, and 10%-20% for both validation and testing.

Determining how the model learns is a function of the learning rate, the optimizer function, and the loss function. The learning rate dictates how aggressively the model will re-weight its parameters based on iterative feedback after each training step. The optimizer function dictates the approach the model uses to converge on the global minimum. The loss function is the measure the model uses to assess its performance after each training run. Overall, the model's objective is to evolve after each training iteration to find the lowest loss. Other terminology includes the epoch number (number of training iterations) and the batch size (the number of inputs processed in a single step). Once the model has been fully trained, it is the researcher's responsibility to find the most suitable function to determine the overall accuracy, which may not necessarily be the same as the loss function. These factors can all influence model performance.

2.6 Ongoing challenges with ablative therapies

While minimally invasive ablative therapies have considerable promise, their flexibility is also be one of their pitfalls. As discussed previously, researchers have investigated vastly different treatment plans to treat PCa, ranging from focal to whole-gland ablation. The decision how much prostate to ablate is a delicate interplay between i) the properties of the ablation device, such as depth of penetration and physical access ii) the individual disease characteristics, such as the grade and size of index lesion and if it is multi-focal iii) the tolerance for adverse events in case of overtreatment and iv) the patient wishes. This complexity is one reason why there is no established consensus which ablation coverage is optimal. Furthermore, the variable ablation coverages make it difficult to compare results between studies.

Follow-up after ablative therapy is another challenge. As discussed previously, conventional therapies such as RP and EBRT use the well-accepted PSA value as a marker for recurrence (Mottet et al., 2022). Yet the definition of treatment success for ablative therapies is much less clear. Recent efforts have tried to formalize monitoring after ablative therapy, recommending a combination of post-treatment biopsies, PSA monitoring and imaging (Becher & Lepor, 2020; Lebastchi et al., 2020). Nevertheless, this multi-faceted follow-up schedule does not standardize what is considered treatment success. This applies to both treatment-naïve and radiorecurrent PCa. The absence of any randomized control trials makes it difficult to assess the oncological efficacy of any given ablative therapy compared to conventional therapies (Mottet et al., 2022).

Specifically in the context of radiorecurrent disease, current evidence from PSMA-PET/CT imaging indicates that only 18-40% of recurrences are purely local (Maitre et al., 2022). Ablative therapies are not well-suited to treating disease which has extended beyond the prostate, and distant metastases are generally untreatable. Furthermore, even if purely local recurrence is suspected on imaging, the prostate and surrounding tissues undergo considerable anatomical changes after radiation, making it harder to rule out presence of non-local lesions (Koopman et al., 2020; Vargas et al., 2012). When combined with the knowledge that radiorecurrent PCa is intrinsically more aggressive disease (Williams & Hu, 2013), this ultimately reduces the number of eligible patients for local ablative salvage therapies and further decreases the likelihood of complete disease eradication if treatment is offered.

Beyond disease eradication, toxicity of local ablative salvage therapies must also be considered. Patients with radiorecurrent PCa are typically older, and inherently more prone to adverse events. The irradiated prostate and surrounding anatomy are also more sensitive than treatment-naïve tissues, which explains the high toxicity rates seen in other local ablative salvage series (Ingrosso et al., 2020). The benefit of any local salvage therapy must always be balanced against the safety risks.

3 Aims

The aims of this doctoral thesis were three-fold:

I. Using retrospective TULSA treatment MRI images, the first aim was to investigate the impact of residual fiducial markers on the immediate salvage TULSA ablation outcome. Investigate their local susceptibility artifact, their ability to block ultrasound heating, and their distribution in the prostate. Determine treatment planning guidelines based on these findings. When one considers the lower odds of purely localized radiorecurrent disease, the ability to successfully ablate all targeted prostate tissue, even in the presence of fiducial markers, is therefore of considerable importance for this selected patient group.

II. Using retrospective TULSA clinical and imaging data from the same cohort, the second aim was to determine if gold fiducial markers had an impact on both safety and early-stage efficacy of salvage TULSA treatment. Depending on disease characteristics and patient wishes, perform focal to whole-gland ablation, with the key objective to target the disease while reducing toxicity, particularly in this more at-risk and elderly patient population. Monitor safety using functional questionnaires and adverse events. To monitor early-stage treatment success, use a combination of post-therapy biopsies, imaging, and PSA monitoring. While emerging devices for treatment of localized radiorecurrent disease may be promising, it is essential to rigorously investigate their safety and efficacy for this vulnerable patient group.

III. The inability to predict the post-treatment non-perfused volume after ablative therapy is a significant limitation to any ablative therapy, as it prevents immediate re-treatment. The third aim was therefore to develop a deep learning model that uses contrast-free TULSA treatment-day MRI images as inputs and generates synthetic post-treatment CE-enhanced images of the ablation outcome, with an accuracy comparable to ground truth.

4 Materials and Methods

4.1 Patients

In Study I, nine patients with local radiorecurrent PCa who underwent salvage TULSA (sTULSA) between November 2018 and October 2020 were included in the study (NCT03350529). The same nine-patient cohort was included in Study II, save for one patient with locally advanced PCa, who was omitted. All nine patients had residual fiducial markers from previous radiation therapy and were composed of either gold or nitinol. A detailed summary of marker types and composition is provided in Table 4. In Study II, a control cohort of thirteen patients from the same trial but without fiducial markers who underwent sTULSA was also included. This control cohort was gathered to facilitate comparison of post-sTULSA safety for patients with and without fiducial markers. Table 5 provides a detailed summary of patient characteristics in Studies I and II.

Table 4. Summary of fiducial marker properties for nine patients studied (Modified from original publication I)

Marker type, size	Marker material	Number of patients
BeamMarks, 1.2x5mm	Nitinol	1
GoldLock, 1x3mm	Gold	5
GoldLock, 1x5mm	Gold	2
QLRAD, 1.2x3mm	Gold	1

Across the nine patients, twenty-two total markers were left inside the prostate after prior radiation therapy. Of these 22 total markers, 20/22 (91%) were located directly in the ultrasound line-of-sight and therefore could have theoretically impacted the ultrasound heating.

Table 5. Patient characteristics and disease history before sTULSA: target group with markers vs. control group (Modified from original publication II)

ID	Year of diagnosis	Gleason grade group	PSA, ng/ml	Primary treatment, Gy	Age at time of sTULSA, years	Time from primary therapy to sTULSA, years
TARGET GROUP						
T1*				EBRT		
T2	2008	1	9.5	EBRT, 72 Gy	77	130
T3	2008	2	14	EBRT, 76 Gy	70	129
T4	2010	3	22	EBRT, 72 Gy	63	109
T5	2016	5	65	EBRT, 76+24 Gy	67	33
T6	2011	5	15	EBRT, 76 Gy	76	101
T7	2014	1	10	EBRT, 76 Gy	73	68
T8	2014	5	17.6	EBRT, 728 Gy	71	65
T9	2012	2	7.5	EBRT, 76 Gy	72	96
CONTROL GROUP						
C1	2005	1	8.5	EBRT	69	157
C2	2007	1	21	EBRT	69	138
C3	2009	5	9.8	EBRT	69	114
C4	1999	1	13	EBRT	80	237
C5	2015	1	9.4	Brachytherapy	66	48
C6	2004	5	37	EBRT	67	175
C7	2004	1	13	EBRT	81	144
C8	2008	1	47	EBRT	72	132
C9	2004	3	23	EBRT	76	186
C10	2000	1	29	EBRT	74	225
C11	2007	2	23	EBRT	64	155
C12	2003	1	30	EBRT	73	210
C13	2004	5	22	EBRT	72	199

* This patient had locally advanced PCa and was not included in Study II

In Study III, a total of ninety-five patients who underwent TULSA between September 2016 and January 2020 were used to train, validate, and test the deep

learning model. These ninety-five patients spanned three different clinical trials and four different treatment groups (NCT02766543, NCT03814252 and NCT03350529). For all treatment groups, TULSA was their first major prostate therapy. Treatment groups included:

- primary localized PCa, whole-gland ablation (n = 64)
- primary localized PCa, partial ablation (n = 20)
- primary localized PCa, partial ablation with treat and resect intent (n = 5)
- BPH (n = 6)

A summary of the Study III patient characteristics is provided in Table 6.

Table 6. Summary of patient characteristics for those patients used in deep learning model, median (IQR) (Modified from original publication III)

Treatment intent	Age, years	PSA, ng/ml	Gleason score	IPSS
PCa	65 (58-69)	6.5 (5.0-9.1)	6 (n = 26) 7 (n = 60) 8 (n = 3)	n.a.*
BPH	71 (65-72)	3.4 (2.7-3.7)	n.a.*	20 (16-27)

* Not applicable

For studies I, II and III, written informed consent from all participants was provided, local ethics permission was obtained, and all studies were conducted according to the declaration of Helsinki.

4.2 Therapeutic device

For all three studies described in this doctoral thesis, TULSA (TULSA-PRO, Mississauga, Canada) was used as the sole therapeutic device. All treatments were performed on 3 Tesla (T) MRI machines, spanning a range of models and vendors (Achieva/Ingenia, Best, Netherlands) (Skyra, Prisma, Erlangen, Germany).

4.3 MRI protocol

For every TULSA patient, a standardized treatment-day imaging protocol was used. Sequences included:

1. Localizer (initial positioning assessment)
2. Sagittal (SAG) T2 3D (device registration and fine positioning)

3. Axial (AX) T2 (target boundary delineation)
4. AX EPI (basis of thermometry sequence and co-aligned to AXT2)
5. AX CE-T1w (post-treatment assessment of non-perfused volume and co-aligned to AXT2)

To compute thermometry, both the magnitude (MAG) and phase components of the EPI sequence were sent to the TULSA computer. The MAG was used to visualize intensity changes, while the phase image was used to compute the PRFS phase differences throughout the ablation. Different processing techniques can be applied to the thermometry images, which can in turn generate three distinct types of image sets:

- Current temperature (the current temperature at each pixel)
- Maximum temperature (TMax), the maximum temperature at each pixel since treatment start
- Thermal dose (TDose), the accumulated thermal dose at each pixel since treatment start

Post-treatment CE-imaging was performed in two steps. First, a native T1w sequence without contrast was acquired. Thereafter, GBCA was injected into the bloodstream, followed by the same T1w sequence with contrast. A final subtraction (SUB) image was used to evaluate the non-perfused volume. A detailed summary of the TULSA sequence protocol is provided in Table 7.

Table 7. TULSA sequence protocol summary (Modified from original publication I)

Name	TR, ms	TE, ms	Flip angle, deg	FOV†, mm	Slice thickness, mm	Resolution, mm	Slice Spacing, mm	EPI factor	Update rate, s
AX T2w	7500	101	160	260x260	3	0.8 x 0.8 x 3	5	n.a.*	n.a.*
AX EPI	25	7.6	12	256x256	4.6	0.8 x 0.8 x 3	5	11	6
AX T1w	704	14	120	260x260	3	0.8 x 0.8 x 3	5	n.a.*	n.a.*

* Not applicable
† Field-of-view

4.4 Safety and early-stage efficacy monitoring

Safety

Safety was monitored for all patients included in Study II, both in the target (with fiducial markers) and control (without fiducial markers) cohort. Patients were followed up to one year. AEs were recorded according the Clavien-Dindo Classification of Surgical Complications. Functional outcomes were collected at baseline and at 3-month intervals, and included the EPIC-26, IIEF-5, IPSS and IPSS-QoL questionnaires.

Early-stage efficacy

To assess the early-stage efficacy of TULSA treatment of the target group in Study II, three metrics were used and recorded up to one year after treatment, including: PSA, imaging, and histopathology. PSA measurements were performed at baseline and thereafter in 3-month intervals. Control MRI imaging was performed during screening, three months post-TULSA and at 12 months. At 12 months, PSMA-PET/CT was also performed using the ^{18}F-PSMA-1007 labeled marker. Tumor uptake was evaluated by monitoring the maximum standard uptake value.

Once all imaging was completed at the 12-moth follow-up, ultrasound-guided transrectal cognitive-targeted biopsies were given to confirm the histopathological extent of disease. The number of cores taken depended on the size of the gland and if any regions of local recurrence from MRI or PSMA-PET/CT imaging were deemed suspicious by the radiologist, both in-/out-of-field.

4.5 Image analysis

A variety of analyses were performed on TULSA images. Prostate volume and non-perfused volume contouring was performed on the AX T2 and CE-T1w sequences with contrast, respectively, using AW Server software (AW Server 3.2, GE Healthcare, Chicago, Illinois, United States). Since the position of the fiducial marker likely influenced its ability to distort ultrasound, the location of all fiducial markers inside the prostate was measured using two metrics including a) the distance from fiducial marker to prostatic urethra center and b) the distance from fiducial marker to prostate capsule.

In Study I, susceptibility artifacts were contoured on the screening AX T2, native T1w, DWI, and thermometry sequences using Mango software (Mango/UTHSCSA, San Antonio, Texas, United States). Susceptibility artifacts were contoured where visible for each applicable slice. To avoid bias, manual segmentation was done

randomly and blinded across patient number, sequence, and implant type. Susceptibility artifact volume, length, width, and orientation were calculated for each marker. Susceptibility artifact segmentation is illustrated in Figure 15.

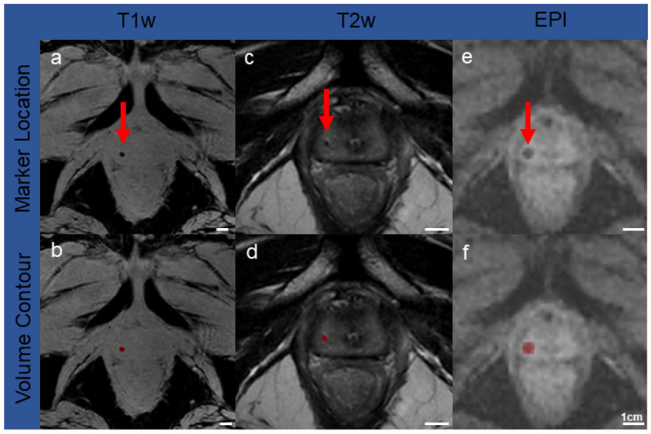

Figure 15. Demonstration of susceptibility artifact segmentation for three different MRI sequences for a gold marker (From original publication I)

Continuing with the methodology employed in Study I, two techniques were employed to quantify the disturbance of fiducial markers on ultrasound heating. The first technique measured the thermal dose accumulation directly behind the marker in the direct line-of-sight of the ultrasound beam. The difference between the 240 CEM isodose line measured in relation to the target boundary in millimeters was measured for all markers. If the value was negative, this indicated undertreatment. All thermal analysis was performed using MATLAB (MathWorks, Natick, Massachusetts, United States). This measurement technique is demonstrated in Figure 16.

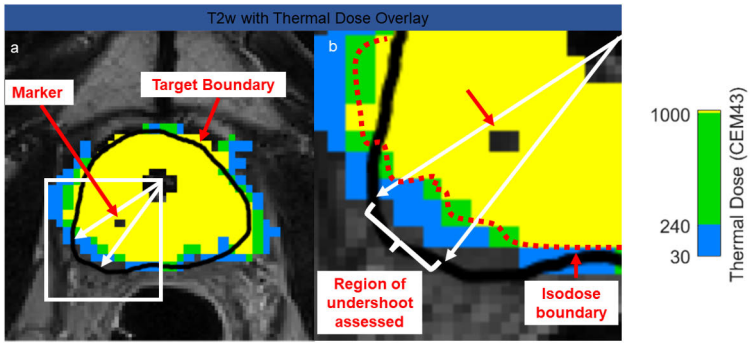

Figure 16. Demonstration of marker-induced thermal undershoot (From original publication I).

Due to the inherent challenges of MRI thermometry, a second objective technique was used to assess marker-induced undertreatment. Post-treatment CE-T1w imaging with GBCA was acquired at various time points, including immediately after treatment, and then repeated at 3- and 12-months. The amount of enhancing tissue behind each marker was recorded. This is illustrated in Figure 17.

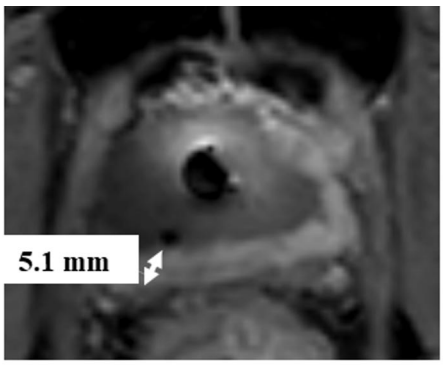

Figure 17. Measurement of residual enhancing tissue behind fiducial marker (Modified from original publication II).

4.6 Deep learning model

Data preparation

All methods referring to deep learning refer to Study III. Five unique TULSA treatment-day sequence types were passed as inputs to the model (T2w, MAG, TMax, TDose, and native T1w). Ground truth consisted of a CE SUB image. Model output was a synthetic SUB CE image.

All treatment-day imaging data that was passed to the deep learning model were resampled to an in-plane resolution of 1x1mm, and then center-cropped to 128x128mm. The T2w, MAG and T1w images (both native and SUB) were clipped to remove outliers, adjusted to have zero mean and a variance of one, and then rescaled from 0 to 1. For the temperature images, the TMax and TDose images were clipped from 35 to 85°C and 0 to 10000 CEM43, respectively, and then rescaled from 0 to 1. Any imaging slice that did not include ablated prostate was discarded. For each included slice, a corresponding physician-drawn prostate mask was also included. No data augmentation was applied.

Model description

The deep learning model used was based on the 2D UNet architecture. Training and validation were done on a graphics processing unit with the Tensorflow package implemented in Python. The ratio of train, validation and test was 80%, 10% and 10%, respectively. Within each group, a ratio of 2:1 whole-gland to partial ablation was kept. Descriptions of the 2D UNet model architecture, inputs, outputs, and ground truth are summarized in Figure 18. In total, there were:

- Train dataset: 75 total patients with 2505 inputs and 501 outputs
- Validation dataset: 10 total patients with 325 inputs and 65 outputs
- Test dataset: 10 total patients with 360 inputs and 72 outputs

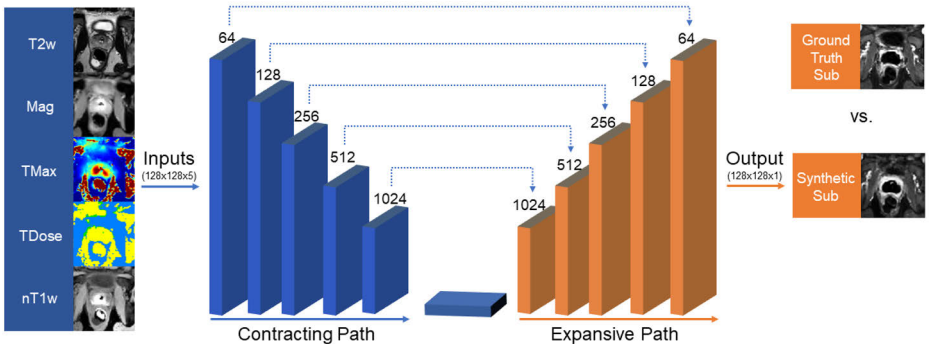

Figure 18. 2D UNet model summary (From original publication III)

Custom loss function

During training and validation, a custom loss function was created that was used to minimize the loss between ground truth and synthetic SUB images after every epoch. It was a composite of three different loss functions including the mean absolute error (MAE), structural similarity index (SSIM) and prostate mask loss P1, whereby P1 was unique to each slice in the dataset. The prostate mask loss was identical to the MAE, except that those pixels outside the prostate were set to 0. The custom loss function is described below:

$$\boldsymbol{loss} = \boldsymbol{\lambda_1} * \boldsymbol{MAE} + (\boldsymbol{\lambda_2} * (\boldsymbol{1} - \boldsymbol{SSIM})) + (\boldsymbol{\lambda_3} * \boldsymbol{P1}) \quad \textbf{(5)}$$

The coefficients λ_1, λ_2 and λ_3 were set to 1 for the first 40 epochs of training. To optimize the model inside the prostate, the coefficients were updated to λ_1 and λ_2 to 0.1 and λ_3 to 10 for another 40-epoch run. The run with the lowest validation loss

and the corresponding weights was used. All training was done with the Adam optimizer, a learning rate of 1e-4 and a batch size of 12.

Model evaluation metrics

Accuracy of entire synthetic SUB image compared to ground truth SUB was evaluated on all test slices using four different quantitative measures including MAE, SSIM, mean squared error (MSE) and peak signal-to-noise ratio (PSNR). This analysis was repeated, but with emphasis on the prostate, by setting all values outside the prostate mask to zero.

In addition to the global quantitative metrics, the accuracy of the non-perfused volume between the synthetic SUB and ground truth SUB images was calculated using the Dice-Similarity Coefficient (DSC). To compute this, the non-perfused volume for all test synthetic and ground truth slices were contoured and then compared head-to-head (Figure 19).

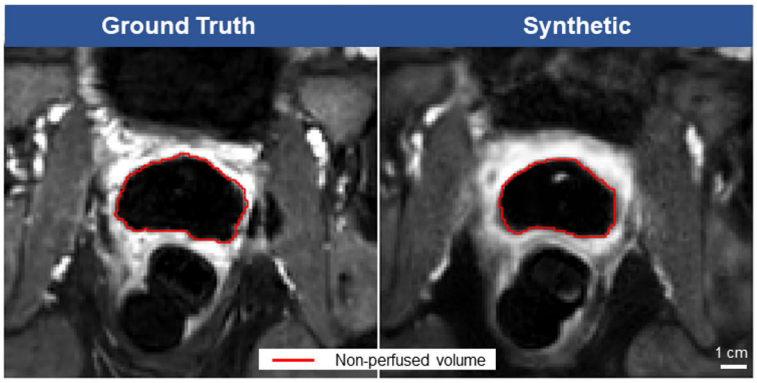

Figure 19. The non-perfused volume was contoured for all ground truth and synthetic subtraction CE-images in the test dataset. Accuracy of the predicted non-perfused volume was then assessed by computing the DSC for both contours. (From original publication III)

Sensitivity analysis

To determine which sequence, if any, was the strongest predictor of the non-perfused volume, a sensitivity analysis was performed. The deep learning model was retrained but inputs were systematically omitted and changes in the resulting DSC were monitored.

Qualitative analysis of prediction

In addition to quantitative assessment of model performance, a radiologist also assessed the overall synthetic image quality. The radiologist was also asked about image quality in the prostate and its surrounding anatomy, such as the rectum and pelvic floor muscles. Finally, they were asked to comment if the predicted non-perfused volume was indistinguishable from ground truth.

4.7 Statistical analysis

For Study II, the statistical software JMP was used. Normality assumptions were confirmed using a quantile plot, kurtosis/skewness evaluation and the Shapiro-Wilk test. A two-tailed t-test was used for significance testing.

For Study III, the 95% confidence intervals were calculated according to Conover (Conover, 1980), while significance testing was done using the non-parametric Wilcoxon rank-sum test.

5 Results

5.1 Technical outcomes for patients with fiducial markers (Study I)

Susceptibility artifact

Independent of marker material, the susceptibility artifact was most pronounced on the thermometry and DWI, followed by the T1w and then finally the T2w. Nitinol markers produced volumetric artifacts that were an order of magnitude larger than the gold markers on the same corresponding MRI sequences. For example, nitinol and gold markers generated volumetric artifacts of 1400 mm^3 and 250 mm^3. For the nitinol markers, the artifact length and width on thermometry increased by factors of 2.6 and 10, respectively, in relation to its actual size.

For gold markers the effect was less pronounced, increasing by average factors of 1.5 and 3.9, respectively, compared to its actual size. As most markers were located perpendicular to B_0, it was not possible to evaluate the impact of marker orientation on artifact size. However, one patient did have two gold markers situated both parallel and perpendicular to B_0. It was found that the marker located perpendicular produced a larger artifact, with a 20% larger length and 86% larger width, compared to the same marker located parallel to B_0. Figure 20 shows the difference in artifact size between nitinol and gold markers.

Distribution inside the prostate

Most fiducial markers were situated: at least 10 mm away from the prostatic urethra center (17/20, 85%), within 10 mm of the prostate capsule (17/20, 85%), and posterior to the prostatic urethra (19/20, 95%). Figure 21 shows the distribution of markers inside the prostate.

Effect on ablation outcome

For regions of prostate that were ablated but did not have any markers in the ultrasound line-of-sight, it was found that the 240 CEM isodose line tended to extend

beyond the target boundary. Across all nine patients studied, this mean (std) value was 2.1 ± 1.6 mm outside the target boundary.

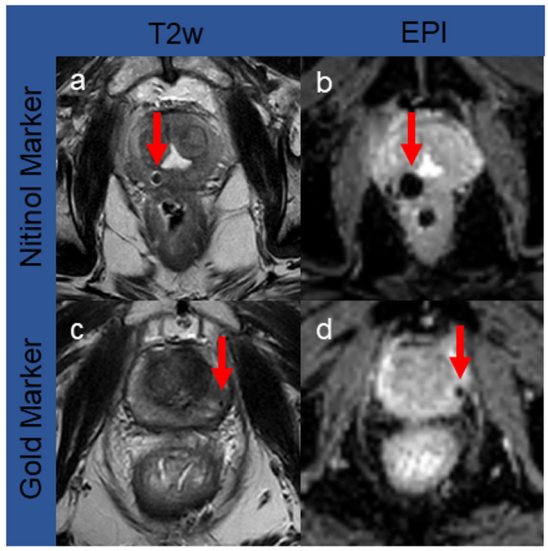

Figure 20. Difference in susceptibility artifact size for nitinol and gold fiducial markers (From original publication I)

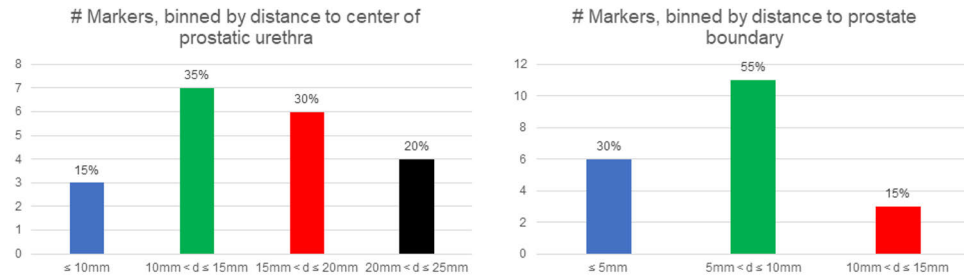

Figure 21. Distribution of fiducial markers inside the prostate (From original publication I)

It was found that 6/20 (30%) markers negatively impacted the treatment outcome, with confirmation from the thermal dose accumulation, acute and 3-month CE-imaging findings.

Four of the six markers caused undertreatment due to their local susceptibility artifact. Both nitinol markers created large artifacts which corrupted a sizable portion of the thermometry image. These large artifacts forced the physician to inwardly adjust their boundary until the target boundary was beyond the reach of the artifact, leading to expected but undesired undertreatment. This was confirmed on both

immediate and 3-month CE-imaging. Two gold markers were also responsible for undertreatment, resulting from their positioning inside the prostate. Both gold markers were situated less than four millimeters from the target boundary. The small but detectable artifacts resulted in false positive temperature readings, and the TULSA controller mistakenly shut off power during these angular sectors, due to a belief that the target boundary had been sufficiently treated. However, the immediate and 3-month CE-imaging findings revealed persistent enhancing tissue behind the marker. Otherwise, there was a strong correlation between the thermal dose accumulation and the 3-month control CE-imaging. Figure 22 highlights a successful and unsuccessful case.

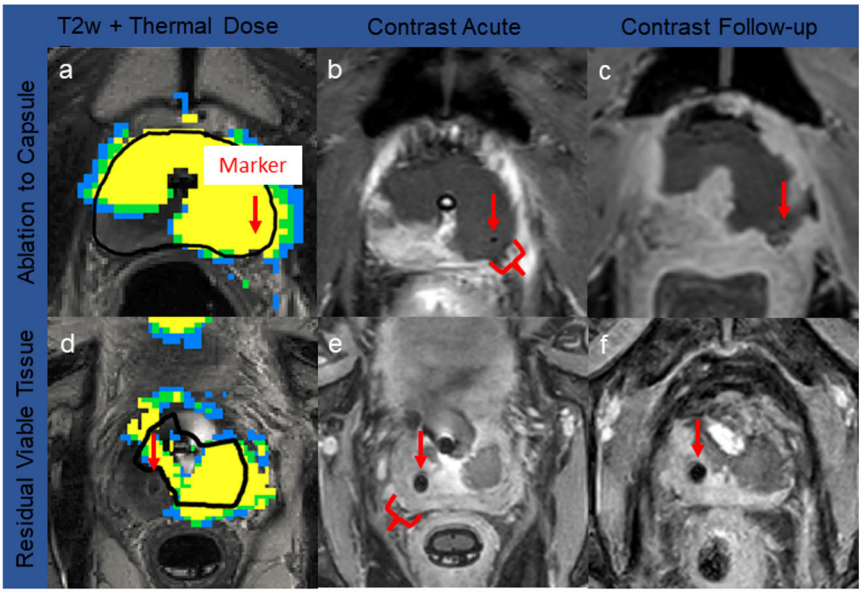

Figure 22. Good thermal dose accumulation behind gold marker (a), confirmed on CE-imaging acute (b) and 3-month follow-up (c). Poor thermal dose accumulation behind a nitinol marker (d), confirmed with CE-imaging immediately (e) and at the next follow-up (f), confirmed by significant residual enhancing tissue behind the marker. (From original publication I)

Two additional gold markers caused undertreatment by blocking the ultrasound heating, which was observed on both the temperature and CE-imaging findings. These two markers were uniquely situated, located simultaneously close to the prostatic urethra (<12 mm) and far from the target boundary (<13mm). Figure 23 highlights two cases where markers caused large undertreatment visible on thermal dose image.

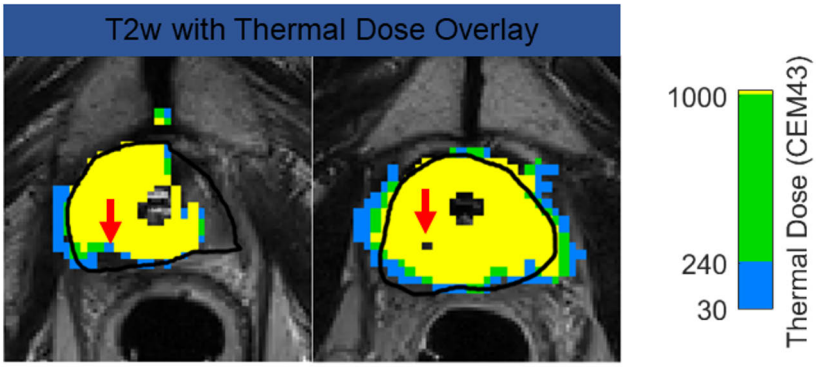

Figure 23. Two different examples where unique location of marker inside prostate contributed to significant undertreatment, which could be seen on the thermal dose map during the ablation. (Modified from original publication I)

5.2 Effect of fiducial markers on safety and early-stage efficacy (Study II)

Adverse events and functional outcomes

From the eight-patient marker group, one grade 3 (whole-gland), three grade 2 (2 whole-gland and 1 partial) and one grade 3 (whole-gland) AE was reported. Three patients had urinary tract infections which resolved with oral antibiotics. One patient had both urinary infection and retention, which required prolonged suprapubic catheterization. The most significant grade 3 event was a fistula formation extending to the symphytic joint with osteitis, which required long-term peroral antibiotic treatment and prolonged catheterization. From the 13-patient control group, two grade 3 (all whole-gland) and four grade 2 (3 whole-gland, 1 partial) AEs were found. Grade 2 events included urinary tract infections and prolonged catheterization. Grade 3 events included J-stent insertion and a urethral stricture.

By 12 months, the marker group reported an average 116%, 14%, and 45% deterioration in EPIC-26 urinary incontinence, EPIC-26 irritation/bother and IPSS, respectively. All other domains were largely unaffected. When accounting for ablation type, no statistical differences between cohorts for either AE or functional outcomes was found, since most patients with markers (6/8, 75%) underwent whole-gland treatment, while only 6/13 (46%) patients without markers underwent whole-gland therapy.

PSA, imaging, and histopathology

In the target cohort, the average PSA decreased by 97% at 12 months compared to baseline. One of eight patients (13%) had rising PSA at three months post-TULSA.

Suspicion of local recurrence after TULSA varied according to imaging modality. For one patient, the 12-month MRI imaging suggested local recurrence on DWI, despite negative PSMA-PET/CT and biopsy findings afterwards. Three recurrences outside the prostate were suspected using PSMA-PET/CT after TULSA. This included positive findings for one patient outside the prostate, with uptake observed in the seminal vesicle, parailiacal lymph nodes and bone. For the other two patients, uptake in the seminal vesicle was observed.

Only six patients underwent targeted biopsies, and all were negative. Figure 24 highlights a successful case.

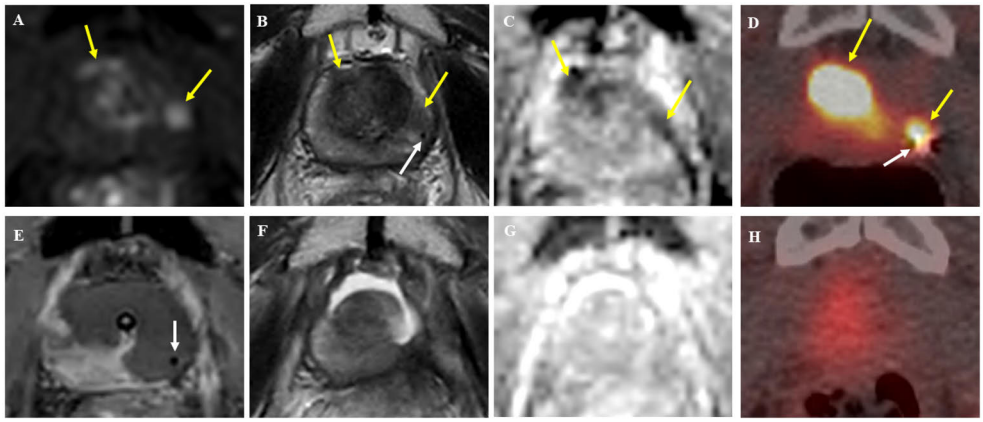

Figure 24. Baseline MRI imaging revealed two index lesions, seen by early enhancement (a), hypo-intensity (b) and diffusion restriction (c), while PSMA-PET/CT revealed concordant uptake (d). CE-imaging immediately after TULSA (e) revealed non-perfused volume extending to prostate capsule. MRI imaging at 12 months revealed a fluid-filled cavity (f) and the absence of any diffusion restriction (g). PSMA-PET/CT imaging at 12 months showed no regional uptakes and the disappearance of the markers inside the prostate. (From original publication II)

Prostate volume, non-perfused volume, and marker disappearance

Considerable changes in prostate volume were observed at 3- and 12-months post-TULSA compared to baseline, with average decreases of 22% and 78%, respectively. Based on CE-imaging, the amount of enhancing tissue behind markers decreased over time. There was leftover enhancing tissue for 13/18 (72%), 3/18 (17%) and 2/18 (11%) of markers immediately, at 3- and 12-months post-TULSA, respectively. Over half of the fiducial markers had disappeared by 12 months (11/18, 61%). Three markers were attached to periprostatic fibrous tissue, three were

encapsulated within the non-perfused volume and two were still located within viable prostate tissue.

5.3 Accuracy of deep learning CNN model (Study III)

Quantitative outcomes

The similarity between ground truth and synthetic CE SUB images for the test dataset according to different metrics is described in Table 8. For the whole image comparison, the average MSE (0.04), yet the SSIM and MAE did not score high (0.34 and 0.14, respectively). Restricting the analysis to the prostate itself, the metrics improved considerably, with average SSIM and MAE scores of 0.93 and 0.02, respectively. The mean (std) DSC between synthetic and ground truth non-perfused volume was 85% ± 8.1%, with 95% confidence intervals of 84% and 88%.

Accuracy of the predicted non-perfused volume was correlated to the size of the prostate radius being treated, with significantly better non-perfused volume predictions occurring when the prostate radius was greater than 24 mm ($p < 0.001$). non-perfused volume prediction was significantly better on whole-gland vs. partial ablation slices ($p < 0.001$).

Table 8. Image similarity for test dataset, ground truth vs. synthetic CE-images, mean (std) (Modified from original publication III)

	SSIM (0 to 1)	**PSNR (dB)**	**MAE (0 to inf)**	**MSE (0 to inf)**
Whole image	0.34 ± 0.13	14.45 ± 2.18	0.14 ± 0.05	0.04 ± 0.02
Prostate only	0.93 ± 0.04	22.23 ± 2.51	0.02 ± 0.01	0.01 ± 0.004

Sensitivity analysis

The best performance was observed when the model trained with all five image inputs. However, the model performance did not significantly deteriorate when trained without the T1w, TMax and TDose inputs. Performance was affected however when the model was trained with only the T2w and MAG inputs.

Qualitative outcomes

The radiologist found that synthetic CE-images tended to be blurrier than their ground truth counterparts, and image quality was sub-optimal near the apex and

bladder. Inside the prostate itself, the predicted non-perfused volume was consistently smoother and less jagged. Overall, the predicted non-perfused volume was indistinguishable from ground truth in 22/72 (31%) of test slices. The predicted non-perfused volume had a bias towards underestimation (36/72, 50%) compared to overestimation (14/72, 19%). Figure 25 is a depiction of model performance for three different test slices.

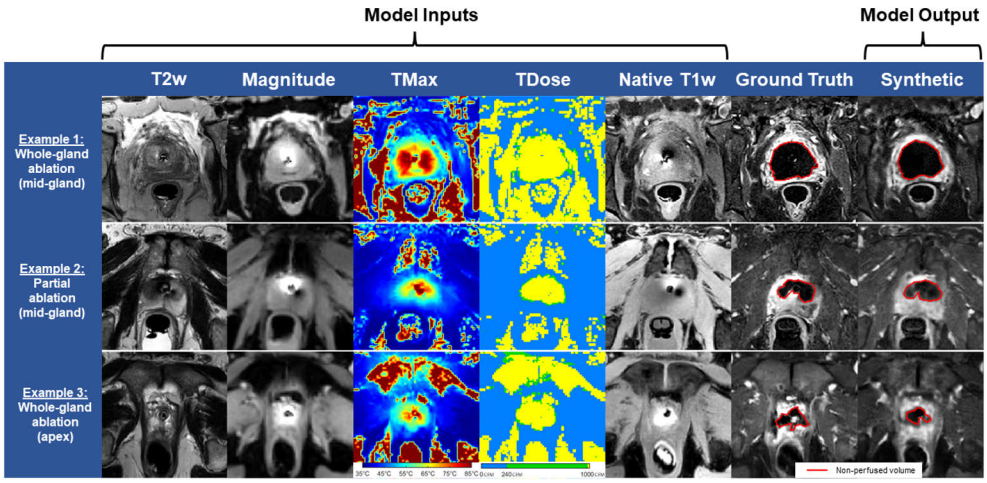

Figure 25. Model performance for three different test slices. (From original publication III)

The model correctly predicted overshoot into the pelvic floor muscles in just under half of all cases where it occurred (6/15, 40%), despite being optimized to minimize the loss inside the prostate. The model also incorrectly predicted overshoot into rectal wall for one patient, which occurred because the model was unable to recognize the difference between non-enhancing tissue and an air bubble, which appeared mid-treatment.

6 Discussion

6.1 Effect of fiducial markers on TULSA therapy

In Studies I and II, both the technical and clinical impact of fiducial markers on sTULSA therapy for radiorecurrent PCa was investigated. Several key findings warrant further discussion.

Technical outcomes

In Study I, it was observed that the marker composition played a significant role on the induced MRI susceptibility artifact. Particularly on thermometry, nitinol markers produced large blooming artifacts that were an order of magnitude larger than gold makers. Nitinol markers are nickel titanium alloys, and these alloys are strongly paramagnetic, and induce sharp local field inhomogeneities. Nitinol artifacts obscured a considerable extent of the nearby anatomy, making accurate thermometry unfeasible. The physician had to adjust the intended target boundary inwards before treatment began, leading to substantial undesired but expected undertreatment. Patients with nitinol markers undergoing sTULSA should be thoroughly screened before being enrolled.

Conversely, TULSA treatment was generally not hampered by gold fiducial markers. Nevertheless, of the 18 gold markers studied, four lead either indirectly or directly to undershoot. While the artifact was less pronounced for gold markers, they still produced detectable susceptibility artifacts, consistent with other studies (Mougenot & Moonen, 2017). Two markers indirectly causing undertreatment were situated close to the target boundary. In these regions, thermal dose measurements suggested sufficient thermal dose had accumulated behind the marker. Upon detailed review, it was observed that the TULSA treatment controller was perturbed, and no acoustic power was delivered in the line-of-sight of the marker. This was later confirmed on CE-imaging with enhancing tissue observed behind the markers. These findings indicate that physicians should be wary of markers near the target boundary and should consider making small millimeter outward adjustments to avoid this artifact. Two other markers located simultaneously close to the urethra (<12mm) and far from the target boundary (>13mm) directly caused undershoot due to an

ultrasound shadowing effect, which was observed directly on thermometry. These were the only markers positioned in this manner, and this undesirable location may have arisen from marker misplacement or migration (O'neill et al., 2016). These results of undershoot are consistent with work done by (Bakaric et al., 2018), who reported that markers located in front of natural transducer focus can result in 100% decrease in lesion size at the intended focus location.

Despite these effects, successful ablation behind the markers was achieved for 14/18 (78%) gold markers. Most markers were located posterior to the urethra and a considerable distance away, likely to prevent voiding (O'neill et al., 2016). The lack of active heating directly behind the marker was compensated by heat dissipation around the marker and thermal diffusion from neighboring unaffected tissue. These results are consistent with other studies which concluded that larger ablation volumes, such as generated during TULSA, can more effectively overcome any ultrasound heating losses from markers (Bakaric et al., 2018; Mougenot & Moonen, 2017).

Finally, these results indicated that 240 CEM43 strongly correlates with the 3-month CE-imaging findings for patients undergoing radiorecurrent PCa treatment with TULSA. This result is consistent with other findings that the full extent of cell kill can take several weeks (Anttinen et al., 2019; Burtnyk et al., 2015). These results can be generalized to many other applications, including MRI-guided biopsy procedures (Fütterer et al., 2016), MRI-guided therapies for radiorecurrent PCa (M. Zhu et al., 2017), and those who receive urological clips for treatment of BPH (Persaud et al., 2019; Roehrborn et al., 2017).

Clinical outcomes

There are several reasons to suspect that fiducial markers could negatively impact TULSA therapy. First, markers can block ultrasound from reaching tissues behind it (Bakaric et al., 2018; Georgiou et al., 2017), leading to undertreatment. Second, the blocked ultrasound energy can accumulate in front of the marker, leading to localized hot spots (Bakaric et al., 2018) and increased risk of unwanted thermal injury.

For all eight patients studied in Study II, at 12 months post-TULSA therapy, systematic undertreatment caused by gold markers was not observed. By 12 months, the tissues behind 16/18 markers were fully ablated, confirmed by CE-imaging. The exception was in one patient where two markers situated close to the urethra and far from the target boundary showed signs of vital tissue behind these markers. Fortunately, the markers were not located in the tumor location and did not worsen oncological outcome.

The CE-imaging findings after sTULSA were confirmed on imaging and biopsy. Early local control was achieved for all eight patients, except for one patient who

had positive MRI but negative PSMA-PET/CT and biopsy. Confirmed histological recurrences were found outside the prostate, either in the seminal vesicles, lymph nodes or bone. These results highlight the challenge of staging high-risk radiorecurrent PCa. In addition to the imaging and biopsy findings, it was observed that the PSA decreased by 97% and prostate volume decreased by 94% at 12 months for patients undergoing whole-gland ablation, in agreement with other studies (Bonekamp et al., 2019).

In terms of safety and functional outcomes after TULSA, no negative correlation was found between outcomes and patients harboring fiducial markers. One patient with markers did have a serious grade 3 AE, which included a urinary fistula extending to pubic symphysis ultimately inducing osteitis. Subsequent treatment was long-term antibiotics, which spontaneously resolved after 12 months. However, the marker did not contribute to this AE, because it was not situated in the line-of-sight of the symphytic joint. Instead, the suspected cause of the fistula is the ultrasound driving frequency. For this patient, the driving frequency was 4 MHz, which does not attenuate as strongly as high frequency, and likely caused regional hot spots near the pubic bone, compounded by the small retropubic space, ultimately leading to the fistula. In general, the safety profile of TULSA was similar to other local salvage therapies (Ingrosso et al., 2020; Valle et al., 2021). It is expected that as the TULSA technology improves, the toxicity should also improve. Comparisons between cohorts underscored that ablation extent (whole-gland vs. partial gland) is a stronger predictor of toxicity outcome, with whole-gland ablation being considerably more toxic.

It was also observed that by 12 months, 11/18 (61%) of markers had disappeared. For patients that may require a second sTULSA therapy due to persistent local recurrence, this could simplify screening due to increased probability of any ultrasound obstructing objects or local artifacts in the prostate.

6.2 Accuracy of synthetic CE-images generated by AI

Study III established clear feasibility of synthetic CE-image generation based on unenhanced treatment-day TULSA images using deep learning. This is a challenging problem due to the complicated physiological reaction occurring after elevated temperature ablation (Anttinen et al., 2019; Boyes et al., 2007; Staruch et al., 2017), which can lead to irregular shapes of the non-perfused volume. Generally, the model was able to overcome these complexities, recording a mean DSC of 85% between prediction and ground truth. This result is similar to prostate capsule segmentation with newer deep learning techniques (Aldoj et al., 2020; Q. Zhu et al., 2017). Overall,

it was found that the predicted non-perfused volume was indistinguishable from ground truth for one third of all test slices, with a slight bias towards underestimation.

Model performance was significantly better in larger prostates, consistent with other studies (Aldoj et al., 2020; Montagne et al., 2021; Shahedi et al., 2014; Q. Zhu et al., 2017). This is likely a consequence of the higher SNR. Specifically, higher delivered acoustic power translates to increased signal on thermometry and CE-images. The analysis also revealed that no individual image produces statistically significant better non-perfused volume predictions, which has implications for TULSA therapy monitoring. During TULSA therapy, there may be disagreement between the thermal dose and max temperature readings, but these results indicate neither image type is a better predictor of the final non-perfused volume in isolation.

According to radiological review, deep learning synthetic images were blurrier compared to ground truth. Important anatomical structures surrounding the prostate were also less visible, such as the prostate apex and bladder neck. This may have been caused due to variability in the urinary catheterization method employed. The model could predict non-perfused volume outside the prostate but missed approximately 60% of cases where it occurred. An improved loss function that accommodates heating outside the prostate could potentially address this if there is sufficient clinical need.

A deep learning model that can generate accurate non-perfused volume predictions could optimize patient outcomes, a positive result for both patients and physicians. The combination of data augmentation and more patient data is necessary to establish this and requires further exploration.

6.3 Limitations

There were several limitations in this doctoral thesis. In all studies, there was a small patient sample size and patient cohorts were heterogenous. Furthermore, the treatment plans were highly variable, including focal, hemi-. and whole-gland ablation. Importantly, there is also a lack of well-established oncological endpoints for radiorecurrent PCa. There is no clear consensus whether biochemical recurrence, imaging, or biopsies are the gold standard for treatment efficacy. The combination of all these points makes it challenging to assess the efficacy of salvage TULSA treatment, both acutely with respect to the non-perfused volume and longer-term with respect to PSA, imaging, and biopsy endpoints.

Another limitation is that only one deep learning model was used to predict the treatment-day non-perfused volume. While the UNet model is well-established, it is prone to poor performance, especially at sharp edges. Newer state-of-the-art deep learning models could have significantly improved prediction of the non-perfused volume, particularly for partial ablation cases and regions near the urethral and

bladder sphincters. Small sample sizes, variable ablation plans, and patient group heterogeneity likely all contributed to a decrease in overall model performance.

6.4 Future considerations

Another aspect that is challenging for physicians is the assessment of patient eligibility for TULSA. Several factors including prostate size, heterogeneity, density, perfusion, and diffusion could all impact the ablation outcome. One recurring theme for TULSA treatments is the difficulty to heat near the posterolateral corners, which can lead to undertreatment and ultimately recurrence. For certain patients, there is often no obvious rationale why the heating was sub-optimal in this region.

To address this limitation, an approach built on the existing supervised learning AI work could be investigated. For previous TULSA treatments, one could label each treatment slice as well-treated or undertreated. To generate the input layer, one could apply radiomics to those same treatment-day images, which mathematically decomposes images into quantifiable metrics. The various metrics could be passed to an AI model, which then attempts to find correlations between image metrics and undertreatment. If a correlation was found, this would greatly benefit physicians because they could have a higher confidence of TULSA treatment success.

7 Summary/Conclusions

The following conclusions emerge from the studies presented in this thesis:

I. Study I demonstrated that fiducial marker composition strongly influences the associated thermometry artifact. Patients with nitinol markers should be carefully screened to ensure that the marker does not corrupt thermometry. Although an order of magnitude smaller, the susceptibility artifact generated by gold markers is non-negligible. Gold markers can lead to misinterpretations in the accumulated thermal dose when they are located near the target boundary. Study I also demonstrated that marker location inside the prostate strongly determines its effect on ultrasound shadowing, which can cause undertreatment. Gold markers located simultaneously near the prostatic urethra and far from the target boundary are the most likely to induce undershoot. We also confirmed that for ablated fibrotic tissue from prior EBRT, the thermal dose strongly correlates with 3-month CE-imaging findings.

II. Study II demonstrated that radiorecurrent PCa patients with residual gold markers are not at higher risk of incurring AEs or functional outcome degradation compared to those without markers. Nor are these patients likely to experience a decrease in treatment efficacy, as all patients had good local cancer control at their 12-month follow-up. Study II also indicated that by one-year post-TULSA a considerable majority of these markers will be voided by the patient. Finally, this study suggests that a whole-gland ablation of radiorecurrent prostate tissue can negatively impact toxicity compared to partial-gland ablation, warranting further investigation.

III. The findings from Study III indicate that AI can produce realistic synthetic CE-images based on unenhanced image inputs during TULSA therapy, and that this technique has the possibility to improve treatment outcomes. With the combination of a larger training dataset supplemented with data augmentation, this technique has considerable potential. Modern state-of-the-art deep learning models also have the potential to drastically improve model performance.

Acknowledgements

I would like to thank my wife Edina for all the support she gave me throughout these past years and my son Noah, who also put a smile on my face when I most needed it. Of course, this work would not have been possible if I was not surrounded by incredible team members. This includes Mikael Anttinen and Pietari Mäkelä, my supervisors Roberto Blanco Sequeiros and Peter Boström, and of course the rest of the TYKS team. From the Profound team, I would like to thank Alexandre Bigot for his help with deep learning.

February 2023
Cameron Wright

References

Abajian, A., Murali, N., Savic, L. J., Laage-Gaupp, F. M., Nezami, N., Duncan, J. S., Schlachter, T., Lin, M. de, Geschwind, J. F., & Chapiro, J. (2018). Predicting Treatment Response to Intra-arterial Therapies for Hepatocellular Carcinoma with the Use of Supervised Machine Learning—An Artificial Intelligence Concept. *Journal of Vascular and Interventional Radiology*, *29*(6). https://doi.org/10.1016/j.jvir.2018.01.769

Adamy, A., Yee, D. S., Matsushita, K., Maschino, A., Cronin, A., Vickers, A., Guillonneau, B., Scardino, P. T., & Eastham, J. A. (2011). Role of prostate specific antigen and immediate confirmatory biopsy in predicting progression during active surveillance for low risk prostate cancer. *Journal of Urology*, *185*(2). https://doi.org/10.1016/j.juro.2010.09.095

Ahmed, H. U., Arya, M., Freeman, A., & Emberton, M. (2012). Do low-grade and low-volume prostate cancers bear the hallmarks of malignancy? In *The Lancet Oncology* (Vol. 13, Issue 11). https://doi.org/10.1016/S1470-2045(12)70388-1

Aldoj, N., Biavati, F., Michallek, F., Stober, S., & Dewey, M. (2020). Automatic prostate and prostate zones segmentation of magnetic resonance images using DenseNet-like U-net. *Scientific Reports*, *10*(1), 1–17. https://doi.org/10.1038/s41598-020-71080-0

Algaba, F., & Montironi, R. (2010). Impact of prostate cancer multifocality on its biology and treatment. In *Journal of Endourology* (Vol. 24, Issue 5). https://doi.org/10.1089/end.2009.0462

Anttinen, M., Mäkelä, P., Suomi, V., Kiviniemi, A., Saunavaara, J., Sainio, T., Horte, A., Eklund, L., Taimen, P., Sequeiros, R. B., & Boström, P. J. (2019). Feasibility of MRI-guided transurethral ultrasound for lesion-targeted ablation of prostate cancer. *Scandinavian Journal of Urology*, *53*(5), 295–302. https://doi.org/10.1080/21681805.2019.1660707

Anttinen, M., Mäkelä, P., Viitala, A., Nurminen, P., Suomi, V., Sainio, T., Saunavaara, J., Taimen, P., Sequeiros, R. B., & Boström, P. J. (2020). Salvage Magnetic Resonance Imaging-guided Transurethral Ultrasound Ablation for Localized Radiorecurrent Prostate Cancer: 12-Month Functional and Oncological Results. *European Urology Open Science*, *22*, 79–87. https://doi.org/10.1016/j.euros.2020.10.007

Arena, L., Morehouse, H. T., & Safir, J. (1995). MR imaging artifacts that simulate disease: how to recognize and eliminate them. *Radiographics: A Review Publication of the Radiological Society of North America, Inc*, *15*(6). https://doi.org/10.1148/radiographics.15.6.8577963

Arora, R., Koch, M. O., Eble, J. N., Ulbright, T. M., Li, L., & Cheng, L. (2004). Heterogeneity of Gleason grade in multifocal adenocarcinoma of the prostate. *Cancer*, *100*(11). https://doi.org/10.1002/cncr.20243

A.V., D., R., W., S., B. M., D., S., K., B., G.A., B., J.E., T., A.A., R., I., K., & C.J., B. (1998). Biochemical outcome after radical prostatectomy, external beam radiation therapy, or interstitial radiation therapy for clinically localized prostate cancer. *Journal of the American Medical Association*, *280*(11), 969–974. https://doi.org/http://dx.doi.org/10.1001/jama.280.11.969

Bakaric, M., Martin, E., S Georgiou, P., T Cox, B., Payne, H., & E Treeby, B. (2018). Experimental study of beam distortion due to fiducial markers during salvage HIFU in the prostate. *Journal of Therapeutic Ultrasound*, *6*, 1. https://doi.org/10.1186/s40349-018-0109-3

Bamber, J. C. (2004). Attenuation and Absorption. In *Physical Principles of Medical Ultrasonics* (pp. 93–166). John Wiley & Sons, Ltd. https://doi.org/https://doi.org/10.1002/0470093978.ch4

Becher, E., & Lepor, H. (2020). Oncological control following partial gland ablation for intermediate-risk prostate cancer. *Urologic Oncology*, *38*(8), 671–677. https://doi.org/10.1016/j.urolonc.2020.04.017

Bell, K. J. L., del Mar, C., Wright, G., Dickinson, J., & Glasziou, P. (2015). Prevalence of incidental prostate cancer: A systematic review of autopsy studies. *International Journal of Cancer*, *137*(7). https://doi.org/10.1002/ijc.29538

Bill-Axelson, A., Holmberg, L., Garmo, H., Taari, K., Busch, C., Nordling, S., Häggman, M., Andersson, S.-O., Andrén, O., Steineck, G., Adami, H.-O., & Johansson, J.-E. (2018). Radical Prostatectomy or Watchful Waiting in Prostate Cancer — 29-Year Follow-up. *New England Journal of Medicine*, *379*(24). https://doi.org/10.1056/nejmoa1807801

Bolla, M., van Tienhoven, G., Warde, P., Dubois, J. B., Mirimanoff, R. O., Storme, G., Bernier, J., Kuten, A., Sternberg, C., Billiet, I., Torecilla, J. L., Pfeffer, R., Cutajar, C. L., van der Kwast, T., & Collette, L. (2010). External irradiation with or without long-term androgen suppression for prostate cancer with high metastatic risk: 10-year results of an EORTC randomised study. *The Lancet Oncology*, *11*(11). https://doi.org/10.1016/S1470-2045(10)70223-0

Bomers, J. G. R., Cornel, E. B., Fütterer, J. J., Jenniskens, S. F. M., Schaafsma, H. E., Barentsz, J. O., Sedelaar, J. P. M., Hulsbergen-van de Kaa, C. A., & Witjes, J. A. (2017). MRI-guided focal laser ablation for prostate cancer followed by radical prostatectomy: correlation of treatment effects with imaging. *World Journal of Urology*, *35*(5). https://doi.org/10.1007/s00345-016-1924-1

Bomers, J., Wright, C., & Fütterer, J. (2020). *Personalized Treatment for Patients with Prostate Cancer Using MRI-guided Transurethral Ultrasound Ablation (TULSA)*.

Bonekamp, D., Wolf, M. B., Roethke, M. C., Pahernik, S., Hadaschik, B. A., Hatiboglu, G., Kuru, T. H., Popeneciu, I. v, Chin, J. L., Billia, M., Relle, J., Hafron, J., Nandalur, K. R., Staruch, R. M., Burtnyk, M., Hohenfellner, M., & Schlemmer, H.-P. (2019). Twelve-month prostate volume reduction after MRI-guided transurethral ultrasound ablation of the prostate. *European Radiology*, *29*(1), 299–308. https://doi.org/10.1007/s00330-018-5584-y

Borofsky, S., George, A. K., Gaur, S., Bernardo, M., Greer, M. D., Mertan, F. v., Taffel, M., Moreno, V., Merino, M. J., Wood, B. J., Pinto, P. A., Choyke, P. L., & Turkbey, B. (2018). What are we missing? False- negative cancers at multiparametric MR imaging of the prostate. *Radiology*, *286*(1). https://doi.org/10.1148/radiol.2017152877

Boyes, A., Tang, K., Yaffe, M., Sugar, L., Chopra, R., & Bronskill, M. (2007). Prostate Tissue Analysis Immediately Following Magnetic Resonance Imaging Guided Transurethral Ultrasound Thermal Therapy. *Journal of Urology*, *178*(3), 1080–1085. https://doi.org/10.1016/j.juro.2007.05.011

Brace, C. (2011). Thermal tumor ablation in clinical use. *IEEE Pulse*, *2*(5). https://doi.org/10.1109/MPUL.2011.942603

Bratan, F., Niaf, E., Melodelima, C., Chesnais, A. L., Souchon, R., Mège-Lechevallier, F., Colombel, M., & Rouvière, O. (2013). Influence of imaging and histological factors on prostate cancer detection and localisation on multiparametric MRI: A prospective study. *European Radiology*, *23*(7). https://doi.org/10.1007/s00330-013-2795-0

Brierley, J., Gospodarowicz, M. D., & Wittekind, C. T. (2017). TNM Classification of Malignant Tumors International Union Against Cancer. 8th. Oxford, England: Wiley; 2017. Oesphagus including oesophagogastric junction. *Wiley*.

Brown RW, Cheng Y-N, Haacke EM, Thompson MR, & Venkatesan R. (2014). Magnetic Resonance Imaging: Physical Principles and Sequence Design. In *Magnetic Resonance Imaging* (pp. 1–17). John Wiley & Sons, Ltd. https://doi.org/https://doi.org/10.1002/9781118633953.ch1

Bruinsma, S. M., Roobol, M. J., Carroll, P. R., Klotz, L., Pickles, T., Moore, C. M., Gnanapragasam, V. J., Villers, A., Rannikko, A., Valdagni, R., Frydenberg, M., Kakehi, Y., Filson, C. P., Bangma, C. H., Trock, B., Ehdaie, B., Kim, J., Morgan, T., Hyndman, E., … Buzza, M. (2017). Expert consensus document: Semantics in active surveillance for men with localized prostate cancer-

results of a modified Delphi consensus procedure. In *Nature Reviews Urology* (Vol. 14, Issue 5). https://doi.org/10.1038/nrurol.2017.26

Burtnyk, M., Hill, T., Cadieux-Pitre, H., & Welch, I. (2015). Magnetic resonance image guided transurethral ultrasound prostate ablation: A preclinical safety and feasibility study with 28-day followup. *Journal of Urology*, *193*(5). https://doi.org/10.1016/j.juro.2014.11.089

Carstensen, E. L., Child, S. Z., Norton, S., & Nyborg, W. (1990). Ultrasonic heating of the skull. *The Journal of the Acoustical Society of America*, *87*(3), 1310–1317.

Carter, H. B., Kettermann, A., Warlick, C., Metter, E. J., Landis, P., Walsh, P. C., & Epstein, J. I. (2007). Expectant Management of Prostate Cancer with Curative Intent: An Update of The Johns Hopkins Experience. *Journal of Urology*, *178*(6). https://doi.org/10.1016/j.juro.2007.08.039

Catalona, W. J., Richie, J. P., Ahmann, F. R., Hudson, M. A., Scardino, P. T., Flanigan, R. C., DeKernion, J. B., Ratliff, T. L., Kavoussi, L. R., Dalkin, B. L., Waters, W. B., MacFarlane, M. T., & Southwick, P. C. (1994). Comparison of digital rectal examination and serum prostate specific antigen in the early detection of prostate cancer: Results of a multicenter clinical trial of 6,630 men. *Journal of Urology*, *151*(5). https://doi.org/10.1016/S0022-5347(17)35233-3

Cellini, N., Morganti, A. G., Mattiucci, G. C., Valentini, V., Leone, M., Luzi, S., Manfredi, R., Dinapoli, N., Digesu', C., & Smaniotto, D. (2002). Analysis of intraprostatic failures in patients treated with hormonal therapy and radiotherapy: Implications for conformal therapy planning. *International Journal of Radiation Oncology Biology Physics*, *53*(3). https://doi.org/10.1016/S0360-3016(02)02795-5

Chade, D. C., Eastham, J., Graefen, M., Hu, J. C., Karnes, R. J., Klotz, L., Montorsi, F., van Poppel, H., Scardino, P. T., & Shariat, S. F. (2012). Cancer control and functional outcomes of salvage radical prostatectomy for radiation-recurrent prostate cancer: a systematic review of the literature. *European Urology*, *61*(5), 961–971. https://doi.org/10.1016/j.eururo.2012.01.022

Chan, H. P., Samala, R. K., Hadjiiski, L. M., & Zhou, C. (2020). Deep Learning in Medical Image Analysis. In *Advances in Experimental Medicine and Biology* (Vol. 1213). https://doi.org/10.1007/978-3-030-33128-3_1

Chen, C., Raymond, C., Speier, B., Jin, X., Cloughesy, T. F., Enzmann, D., Ellingson, B. M., & Arnold, C. W. (2021). Synthesizing MR Image Contrast Enhancement Using 3D High-resolution ConvNets. *IEEE Transactions on Medical Imaging*, *XX*(Xx), 1–10. http://arxiv.org/abs/2104.01592

Chopra, R., Colquhoun, A., Burtnyk, M., N'djin, W. A., Kobelevskiy, I., Boyes, A., Siddiqui, K., Foster, H., Sugar, L., Haider, M. A., Bronskill, M., & Klotz, L. (2012). MR imaging-controlled transurethral ultrasound therapy for conformal treatment of prostate tissue: Initial feasibility in humans. *Radiology*, *265*(1). https://doi.org/10.1148/radiol.12112263

Chopra, R., Tang, K., Burtnyk, M., Boyes, A., Sugar, L., Appu, S., Klotz, L., & Bronskill, M. (2009). Analysis of the spatial and temporal accuracy of heating in the prostate gland using transurethral ultrasound therapy and active MR temperature feedback. *Physics in Medicine and Biology*, *54*(9). https://doi.org/10.1088/0031-9155/54/9/002

Chu, K. F., & Dupuy, D. E. (2014). Thermal ablation of tumours: Biological mechanisms and advances in therapy. In *Nature Reviews Cancer* (Vol. 14, Issue 3). https://doi.org/10.1038/nrc3672

Coakley, F. v., Hricak, H., Wefer, A. E., Speight, J. L., Kurhanewicz, J., & Roach, M. (2001). Brachytherapy for prostate cancer: Endorectal mr imaging of local treatment-related changes. *Radiology*, *219*(3). https://doi.org/10.1148/radiology.219.3.r01jn46817

Coakley, F. v, Qayyum, A., & Kurhanewicz, J. (2003). Magnetic resonance imaging and spectroscopic imaging of prostate cancer. *The Journal of Urology*, *170*(6 Pt 2), S69-75; discussion S75-6. https://doi.org/10.1097/01.ju.0000094958.23276.c4

Conover, W. J. (1980). *Practical Nonparametric Statistics*. John Wiley and Sons.

Cooperberg, M. R., Pasta, D. J., Elkin, E. P., Litwin, M. S., Latini, D. M., Duchane, J., & Carroll, P. R. (2005). The University of California, San Francisco Cancer of the Prostate Risk Assessment score: A straightforward and reliable preoperative predictor of disease recurrence after radical prostatectomy. *Journal of Urology*, *173*(6). https://doi.org/10.1097/01.ju.0000158155.33890.e7

Cornford, P., Bellmunt, J., Bolla, M., Briers, E., de Santis, M., Gross, T., Henry, A. M., Joniau, S., Lam, T. B., Mason, M. D., van der Poel, H. G., van der Kwast, T. H., Rouvière, O., Wiegel, T., & Mottet, N. (2017). EAU-ESTRO-SIOG Guidelines on Prostate Cancer. Part II: Treatment of Relapsing, Metastatic, and Castration-Resistant Prostate Cancer. *European Urology*, *71*(4), 630–642. https://doi.org/10.1016/j.eururo.2016.08.002

Crouzet, S., Blana, A., Murat, F. J., Pasticier, G., Brown, S. C. W., Conti, G. N., Ganzer, R., Chapet, O., Gelet, A., Chaussy, C. G., Robertson, C. N., Thuroff, S., & Ward, J. F. (2017). Salvage high-intensity focused ultrasound (HIFU) for locally recurrent prostate cancer after failed radiation therapy: Multi-institutional analysis of 418 patients. *BJU International*, *119*(6). https://doi.org/10.1111/bju.13766

Crouzet, S., Chapelon, J. Y., Rouviere, O., Mege-Lechevallier, F., Colombel, M., Tonoli-Catez, H., Martin, X., & Gelet, A. (2014). Whole-gland ablation of localized prostate cancer with high-intensity focused ultrasound: oncologic outcomes and morbidity in 1002 patients. *European Urology*, *65*(5), 907–914. https://doi.org/https://dx.doi.org/10.1016/j.eururo.2013.04.039

Culp, M. B. B., Soerjomataram, I., Efstathiou, J. A., Bray, F., & Jemal, A. (2020). Recent Global Patterns in Prostate Cancer Incidence and Mortality Rates. In *European Urology* (Vol. 77, Issue 1). https://doi.org/10.1016/j.eururo.2019.08.005

Cuocolo, R., Comelli, A., Stefano, A., Benfante, V., Dahiya, N., Stanzione, A., Castaldo, A., de Lucia, D. R., Yezzi, A., & Imbriaco, M. (2021). Deep Learning Whole-Gland and Zonal Prostate Segmentation on a Public MRI Dataset. *Journal of Magnetic Resonance Imaging*, *54*(2), 452–459. https://doi.org/10.1002/jmri.27585

Damianou, C. A., Hynynen, K., & Fan, X. (1995). Evaluation of Accuracy of a Theoretical Model for Predicting the Necrosed Tissue Volume during Focused Ultrasound Surgery. *IEEE Transactions on Ultrasonics, Ferroelectrics and Frequency Control*, *42*(2). https://doi.org/10.1109/58.365232

Damianou, C., & Hynynen, K. (1994). The effect of various physical parameters on the size and shape of necrosed tissue volume during ultrasound surgery. *Journal of the Acoustical Society of America*, *95*(3). https://doi.org/10.1121/1.408550

de Sousa, A., Sonavane, S., & Mehta, J. (2012). Psychological aspects of prostate cancer: A clinical review. *Prostate Cancer and Prostatic Diseases*, *15*(2), 120–127. https://doi.org/10.1038/pcan.2011.66

Dickinson, L., Ahmed, H. U., Allen, C., Barentsz, J. O., Carey, B., Futterer, J. J., Heijmink, S. W., Hoskin, P. J., Kirkham, A., Padhani, A. R., Persad, R., Puech, P., Punwani, S., Sohaib, A. S., Tombal, B., Villers, A., van der Meulen, J., & Emberton, M. (2011). Magnetic resonance imaging for the detection, localisation, and characterisation of prostate cancer: Recommendations from a European consensus meeting. *European Urology*, *59*(4). https://doi.org/10.1016/j.eururo.2010.12.009

Dickinson, L., Arya, M., Afzal, N., Cathcart, P., Charman, S. C., Cornaby, A., Hindley, R. G., Lewi, H., McCartan, N., Moore, C. M., Nathan, S., Ogden, C., Persad, R., van der Meulen, J., Weir, S., Emberton, M., & Ahmed, H. U. (2016). Medium-term Outcomes after Whole-gland High-intensity Focused Ultrasound for the Treatment of Nonmetastatic Prostate Cancer from a Multicentre Registry Cohort. *European Urology*, *70*(4), 668–674. https://doi.org/10.1016/j.eururo.2016.02.054

Donohue, J. F., Bianco, F. J., Kuroiwa, K., Vickers, A. J., Wheeler, T. M., Scardino, P. T., Reuter, V. A., & Eastham, J. A. (2006). Poorly Differentiated Prostate Cancer Treated With Radical Prostatectomy: Long-Term Outcome and Incidence of Pathological Downgrading. *Journal of Urology*, *176*(3). https://doi.org/10.1016/j.juro.2006.04.048

Elster, A. D. (1993). Gradient-echo MR imaging: Techniques and acronyms. In *Radiology* (Vol. 186, Issue 1). https://doi.org/10.1148/radiology.186.1.8416546

Epstein, J. I., Walsh, P. C., Carmichael, M., & Brendler, C. B. (1994). Pathologic and Clinical Findings to Predict Tumor Extent of Nonpalpable (Stage T1 c) Prostate Cancer. *JAMA: The Journal of the American Medical Association*, *271*(5). https://doi.org/10.1001/jama.1994.03510290050036

Fukushima, K. (1980). Neocognitron: A self-organizing neural network model for a mechanism of pattern recognition unaffected by shift in position. *Biological Cybernetics*, *36*(4). https://doi.org/10.1007/BF00344251

Fütterer, J. J., Moche, M., Busse, H., & Yakar, D. (2016). In-Bore MR-Guided Biopsy Systems and Utility of PI-RADS. *Topics in Magnetic Resonance Imaging : TMRI*, *25*(3), 119–123. https://doi.org/10.1097/RMR.0000000000000090

Georgiou, P. S., Jaros, J., Payne, H., Allen, C., Shah, T. T., Ahmed, H. U., Gibson, E., Barratt, D., & Treeby, B. E. (2017). Beam distortion due to gold fiducial markers during salvage high-intensity focused ultrasound in the prostate. *Medical Physics*, *44*(2), 679–693. https://doi.org/10.1002/mp.12044

Gilbert, S. M., Dunn, R. L., Miller, D. C., Montgomery, J. S., Skolarus, T. A., Weizer, A. Z., Wood, D. P., & Hollenbeck, B. K. (2017). Functional Outcomes Following Nerve Sparing Prostatectomy Augmented with Seminal Vesicle Sparing Compared to Standard Nerve Sparing Prostatectomy: Results from a Randomized Controlled Trial. *Journal of Urology*, *198*(3). https://doi.org/10.1016/j.juro.2017.03.133

Gleason, D. F. (1966). Classification of prostatic carcinomas. *Cancer Chemotherapy Reports. Part 1*, *50*(3).

Gong, E., Pauly, J. M., Wintermark, M., & Zaharchuk, G. (2018). Deep learning enables reduced gadolinium dose for contrast-enhanced brain MRI. *Journal of Magnetic Resonance Imaging*, *48*(2), 330–340. https://doi.org/10.1002/jmri.25970

Haglind, E., Carlsson, S., Stranne, J., Wallerstedt, A., Wilderäng, U., Thorsteinsdottir, T., Lagerkvist, M., Damber, J. E., Bjartell, A., Hugosson, J., Wiklund, P., & Steineck, G. (2015). Urinary Incontinence and Erectile Dysfunction after Robotic Versus Open Radical Prostatectomy: A Prospective, Controlled, Nonrandomised Trial. *European Urology*, *68*(2). https://doi.org/10.1016/j.eururo.2015.02.029

Hamdy, F. C., Donovan, J. L., Lane, J. A., Mason, M., Metcalfe, C., Holding, P., Davis, M., Peters, T. J., Turner, E. L., Martin, R. M., Oxley, J., Robinson, M., Staffurth, J., Walsh, E., Bollina, P., Catto, J., Doble, A., Doherty, A., Gillatt, D., … Neal, D. E. (2016). 10-Year Outcomes after Monitoring, Surgery, or Radiotherapy for Localized Prostate Cancer. *New England Journal of Medicine*, *375*(15). https://doi.org/10.1056/nejmoa1606220

Harisinghani, M. G., Barentsz, J., Hahn, P. F., Deserno, W. M., Tabatabaei, S., van de Kaa, C. H., de la Rosette, J., & Weissleder, R. (2003). Noninvasive Detection of Clinically Occult Lymph-Node Metastases in Prostate Cancer. *New England Journal of Medicine*, *348*(25). https://doi.org/10.1056/nejmoa022749

Hazle, J. D., Diederich, C. J., Kangasniemi, M., Price, R. E., Olsson, L. E., & Stafford, R. J. (2002). MRI-guided thermal therapy of transplanted tumors in the canine prostate using a directional transurethral ultrasound applicator. *Journal of Magnetic Resonance Imaging*, *15*(4). https://doi.org/10.1002/jmri.10076

He, X., Bhowmick, S., & Bischof, J. C. (2009). Thermal therapy in urologic systems: A comparison of arrhenius and thermal isoeffective dose models in predicting hyperthermic injury. *Journal of Biomechanical Engineering*, *131*(7). https://doi.org/10.1115/1.3128671

Hectors, S. J. C. G., Jacobs, I., Moonen, C. T. W., Strijkers, G. J., & Nicolay, K. (2016). MRI methods for the evaluation of high intensity focused ultrasound tumor treatment: Current status and future needs. In *Magnetic Resonance in Medicine* (Vol. 75, Issue 1). https://doi.org/10.1002/mrm.25758

Hijnen, N. M., Elevelt, A., & Grüll, H. (2013). Stability and trapping of magnetic resonance imaging contrast agents during high-intensity focused ultrasound ablation therapy. *Investigative Radiology*, *48*(7), 517–524. https://doi.org/10.1097/RLI.0b013e31829aae98

Hijnen, N. M., Elevelt, A., Pikkemaat, J., Bos, C., Bartels, L. W., & Grüll, H. (2013). The magnetic susceptibility effect of gadolinium-based contrast agents on PRFS-based MR thermometry during thermal interventions. *Journal of Therapeutic Ultrasound*, *1*(1), 1. https://doi.org/10.1186/2050-5736-1-8

Hlndman, J. C. (1966). Proton resonance shift of water in the gas and liquid states. *The Journal of Chemical Physics*, *44*(12). https://doi.org/10.1063/1.1726676

Hosny, A., Parmar, C., Quackenbush, J., Schwartz, L. H., & Aerts, H. J. W. L. (2018). Artificial intelligence in radiology. In *Nature Reviews Cancer* (Vol. 18, Issue 8). https://doi.org/10.1038/s41568-018-0016-5

Hövels, A. M., Heesakkers, R. A. M., Adang, E. M., Jager, G. J., Strum, S., Hoogeveen, Y. L., Severens, J. L., & Barentsz, J. O. (2008). The diagnostic accuracy of CT and MRI in the staging of pelvic lymph nodes in patients with prostate cancer: a meta-analysis. *Clinical Radiology*, *63*(4). https://doi.org/10.1016/j.crad.2007.05.022

IARC. (2022). *Data visualization tools for exploring the global cancer burden in 2020*.

Ingrosso, G., Becherini, C., Lancia, A., Caini, S., Ost, P., Francolini, G., Høyer, M., Bottero, M., Bossi, A., Zilli, T., Scartoni, D., Livi, L., Santoni, R., Giacomelli, I., & Detti, B. (2020). Nonsurgical Salvage Local Therapies for Radiorecurrent Prostate Cancer: A Systematic Review and Meta-analysis. *European Urology Oncology*, *3*(2), 183–197. https://doi.org/10.1016/j.euo.2018.12.011

Ishihara, Y., Calderon, A., Watanabe, H., Okamoto, K., Suzuki, Y., Kuroda, K., & Suzuki, Y. (1995). A precise and fast temperature mapping using water proton chemical shift. *Magnetic Resonance in Medicine*, *34*(6). https://doi.org/10.1002/mrm.1910340606

Jalloh, M., Leapman, M. S., Cowan, J. E., Shinohara, K., Greene, K. L., Roach, M. 3rd, Chang, A. J., Chan, J. M., Simko, J. P., & Carroll, P. R. (2015). Patterns of Local Failure following Radiation Therapy for Prostate Cancer. *The Journal of Urology*, *194*(4), 977–982. https://doi.org/https://dx.doi.org/10.1016/j.juro.2015.04.111

Jereczek-Fossa, B. A., Rojas, D. P., Zerini, D., Fodor, C., Viola, A., Fanetti, G., Volpe, S., Luraschi, R., Bazani, A., Rondi, E., Cattani, F., Vavassori, A., Garibaldi, C., Alessi, S., Pricolo, P., Petralia, G., Cozzi, G., de Cobelli, O., Musi, G., Ciardo, D. (2019). Reirradiation for isolated local recurrence of prostate cancer: Mono-institutional series of 64 patients treated with salvage stereotactic body radiotherapy (SBRT). *The British Journal of Radiology*, *92*(1094), 20180494. https://doi.org/10.1259/bjr.20180494

Johnson, D. C., Raman, S. S., Mirak, S. A., Kwan, L., Bajgiran, A. M., Hsu, W., Maehara, C. K., Ahuja, P., Faiena, I., Pooli, A., Salmasi, A., Sisk, A., Felker, E. R., Lu, D. S. K., & Reiter, R. E. (2019). Detection of Individual Prostate Cancer Foci via Multiparametric Magnetic Resonance Imaging. *European Urology*, *75*(5). https://doi.org/10.1016/j.eururo.2018.11.031

Jones, C. U., Hunt, D., McGowan, D. G., Amin, M. B., Chetner, M. P., Bruner, D. W., Leibenhaut, M. H., Husain, S. M., Rotman, M., Souhami, L., Sandler, H. M., & Shipley, W. U. (2011). Radiotherapy and short-term androgen deprivation for localized prostate cancer. *The New England Journal of Medicine*, *365*(2), 107–118. https://doi.org/https://dx.doi.org/10.1056/NEJMoa1012348

Jonsson, J. H., Garpebring, A., Karlsson, M. G., & Nyholm, T. (2012). Internal fiducial markers and susceptibility effects in MRI - Simulation and measurement of spatial accuracy. *International Journal of Radiation Oncology Biology Physics*, *82*(5), 1612–1618. https://doi.org/10.1016/j.ijrobp.2011.01.046

Karavitakis, M., Winkler, M., Abel, P., Livni, N., Beckley, I., & Ahmed, H. U. (2011). Histological characteristics of the index lesion in whole-mount radical prostatectomy specimens: Implications for focal therapy. *Prostate Cancer and Prostatic Diseases*, *14*(1). https://doi.org/10.1038/pcan.2010.16

Khatami, A., Aus, G., Damber, J.-E., Lilja, H., Lodding, P., & Hugosson, J. (2007). PSA doubling time predicts the outcome after active surveillance in screening-detected prostate cancer: results from the European randomized study of screening for prostate cancer, Sweden section. *International Journal of Cancer*, *120*(1), 170–174. https://doi.org/10.1002/ijc.22161

Kleesiek, J., Morshuis, J. N., Isensee, F., Deike-Hofmann, K., Paech, D., Kickingereder, P., Köthe, U., Rother, C., Forsting, M., Wick, W., Bendszus, M., Schlemmer, H. P., & Radbruch, A. (2019). Can Virtual Contrast Enhancement in Brain MRI Replace Gadolinium?: A Feasibility Study. *Investigative Radiology*, *54*(10), 653–660. https://doi.org/10.1097/RLI.0000000000000583

Klotz, L., Pavlovich, C. P., Chin, J., Hatiboglu, G., Koch, M., Penson, D., Raman, S., Oto, A., Fütterer, J., Serrallach, M., Relle, J., Lotan, Y., Heidenreich, A., Bonekamp, D., Haider, M., Tirkes, T., Arora, S., Macura, K. J., Costa, D. N., … Eggener, S. (2020). MRI-guided transurethral ultrasound ablation of prostate cancer. *The Journal of Urology*, 101097JU0000000000001362. https://doi.org/10.1097/JU.0000000000001362

Klotz, L., Vesprini, D., Sethukavalan, P., Jethava, V., Zhang, L., Jain, S., Yamamoto, T., Mamedov, A., & Loblaw, A. (2015). Long-term follow-up of a large active surveillance cohort of patients with prostate cancer. *Journal of Clinical Oncology*, *33*(3). https://doi.org/10.1200/JCO.2014.55.1192

Knopp, M. v., Giesel, F. L., Marcos, H., von Tengg-Kobligk, H., & Choyke, P. (2001). Dynamic contrast-enhanced magnetic resonance imaging in oncology. In *Topics in Magnetic Resonance Imaging* (Vol. 12, Issue 4). https://doi.org/10.1097/00002142-200108000-00006

Koopman, A. G. M. M., Jenniskens, S. F. M., & Fütterer, J. J. (2020). Magnetic Resonance Imaging Assessment after Therapy in Prostate Cancer. *Topics in Magnetic Resonance Imaging*, *29*(1), 47–58. https://doi.org/10.1097/RMR.0000000000000231

Kuroda, K., Oshio, K., Mulkern, R. v., & Jolesz, F. A. (1998). Optimization of chemical shift selective suppression of fat. *Magnetic Resonance in Medicine*, *40*(4). https://doi.org/10.1002/mrm.1910400402

L., D., H., A., N., M., A., F., A., K., C., A., & R., H. (2012). Medium-term outcomes following primary focal therapy using hifu for localized prostate cancer. *Urology*, *80*(3 SUPPL. 1), S162. https://doi.org/http://dx.doi.org/10.1016/S0090-4295%2812%2900880-1

Larmor, J. (1897). LXIII. On the theory of the magnetic influence on spectra; and on the radiation from moving ions . *The London, Edinburgh, and Dublin Philosophical Magazine and Journal of Science*, *44*(271). https://doi.org/10.1080/14786449708621095

Lebastchi, A. H., George, A. K., Polascik, T. J., Coleman, J., de la Rosette, J., Turkbey, B., Wood, B. J., Gorin, M. A., Sidana, A., Ghai, S., Tay, K. J., Ward, J. F., Sanchez-Salas, R., Muller, B. G., Malavaud, B., Mozer, P., Crouzet, S., Choyke, P. L., Ukimura, O., Pinto, P. A. (2020). Standardized Nomenclature and Surveillance Methodologies After Focal Therapy and Partial Gland Ablation for Localized Prostate Cancer: An International Multidisciplinary Consensus. *European Urology*, *78*(3), 371–378. https://doi.org/10.1016/j.eururo.2020.05.018

Litjens, G., Kooi, T., Bejnordi, B. E., Setio, A. A. A., Ciompi, F., Ghafoorian, M., van der Laak, J. A. W. M., van Ginneken, B., & Sánchez, C. I. (2017). A survey on deep learning in medical image analysis. In *Medical Image Analysis* (Vol. 42). https://doi.org/10.1016/j.media.2017.07.005

Lumiani, A., Samun, D., Sroka, R., & Muschter, R. (2021). Single center retrospective analysis of fifty-two prostate cancer patients with customized MR-guided transurethral ultrasound ablation (TULSA). *Urologic Oncology: Seminars and Original Investigations*, *000*, 0–7. https://doi.org/10.1016/j.urolonc.2021.04.022

Luo, Y. H., Xi, I. L., Wang, R., Abdallah, H. O., Wu, J., Vance, A. Z., Chang, K., Kohi, M., Jones, L., Reddy, S., Zhang, Z. S., Bai, H. X., & Shlansky-Goldberg, R. (2020). Deep Learning Based on MR Imaging for Predicting Outcome of Uterine Fibroid Embolization. *Journal of Vascular and Interventional Radiology*, *31*(6). https://doi.org/10.1016/j.jvir.2019.11.032

Maenhout, M., van der Voort van Zyp, J. R. N., Borot de Battisti, M., Peters, M., van Vulpen, M., van den Bosch, M., & Moerland, M. A. (2018). The effect of catheter displacement and anatomical variations on the dose distribution in MRI-guided focal HDR brachytherapy for prostate cancer. *Brachytherapy*, *17*(1), 68–77. https://doi.org/10.1016/j.brachy.2017.04.239

Maitre, P., Sood, S., Pathare, P., Krishnatry, R., Agrawal, A., Rangarajan, V., & Murthy, V. (2022). Timing of Ga68-PSMA PETCT and patterns of recurrence after prostate radiotherapy: Implications for potential salvage. *Radiotherapy and Oncology*, *169*. https://doi.org/10.1016/j.radonc.2022.02.014

Maspero, M., Seevinck, P. R., Willems, N. J. W., Sikkes, G. G., de Kogel, G. J., de Boer, H. C. J., van der Voort van Zyp, J. R. N., & van den Berg, C. A. T. (2018). Evaluation of gold fiducial marker manual localisation for magnetic resonance-only prostate radiotherapy. *Radiation Oncology (London, England)*, *13*(1), 105. https://doi.org/10.1186/s13014-018-1029-7

McCorduck, P., & Cfe, C. (2004). *Machines who think: A personal inquiry into the history and prospects of artificial intelligence*. CRC Press.

McDannold, N. (2005). Quantitative MRI-based temperature mapping based on the proton resonant frequency shift: Review of validation studies. In *International Journal of Hyperthermia* (Vol. 21, Issue 6). https://doi.org/10.1080/02656730500096073

McDannold, N. J., Jolesz, F. A., & Hynynen, K. H. (1999). Determination of the optimal delay between sonications during focused ultrasound surgery in rabbits by using MR imaging to monitor thermal buildup in vivo. *Radiology*, *211*(2). https://doi.org/10.1148/radiology.211.2.r99ma41419

McDannold, N. J., King, R. L., Jolesz, F. A., & Hynynen, K. H. (2000). Usefulness of MR imaging-derived thermometry and dosimetry in determining the threshold for tissue damage induced by thermal surgery in rabbits. *Radiology*, *216*(2). https://doi.org/10.1148/radiology.216.2.r00au42517

McNeal, J. E. (1981). The zonal anatomy of the prostate. *The Prostate*, *2*(1). https://doi.org/10.1002/pros.2990020105

McNeal, J. E., Redwine, E. A., Freiha, F. S., & Stamey, T. A. (1988). Zonal distribution of prostatic adenocarcinoma. Correlation with histologic pattern and direction of spread. *American Journal of Surgical Pathology*, *12*(12). https://doi.org/10.1097/00000478-198812000-00001

McRobbie, D. W., Moore, E. A., Graves, M. J., & Prince, M. R. (2006). *MRI from Picture to Proton* (2nd ed.). Cambridge University Press. https://doi.org/DOI: 10.1017/CBO9780511545405

Mitchell, D. G. (1996). Liver I: Currently available gadolinium chelates. In *Magnetic Resonance Imaging Clinics of North America* (Vol. 4, Issue 1). https://doi.org/10.1016/s1064-9689(21)00552-3

Montagne, S., Hamzaoui, D., Allera, A., Ezziane, M., Luzurier, A., Quint, R., Kalai, M., Ayache, N., Delingette, H., & Renard-Penna, R. (2021). Challenge of prostate MRI segmentation on T2-weighted images: inter-observer variability and impact of prostate morphology. *Insights into Imaging*, *12*(1). https://doi.org/10.1186/s13244-021-01010-9

Mottet, N., Cornford, P., van den Bergh, R., Briers, E., de Santis, M., Gillessen, S., Grummet, J., Henry, A., van der Kwast, T., Lam, T., Mason, M., O'Hanlon, S., Oprea-Lager, D., Ploussard, G., van der Poel, H., Rouviere, O., Schoots, I., Tilki, D., Wiegel, T., … Willemse, P. (2022). EAU-EANM-ESTRO-ESUR-ISUP_SIOG Guidelines on Prostate Cancer. *European Association of Urology*.

Mougenot, C., & Moonen, C. (2017). Magnetic Resonance-guided High Intensity Focused Ultrasound in the presence of biopsy markers. *Journal of Therapeutic Ultrasound*, *5*, 25. https://doi.org/10.1186/s40349-017-0103-1

Mouratidis, P. X. E., Rivens, I., Civale, J., Symonds-Tayler, R., & ter Haar, G. (2019). 'Relationship between thermal dose and cell death for "rapid" ablative and "slow" hyperthermic heating.' *International Journal of Hyperthermia*, *36*(1). https://doi.org/10.1080/02656736.2018.1558289

Mttixer, N., & Reiter, R. C. (1965). Temperature dependence of chemical shifts of protons in hydrogen bonds. *The Journal of Chemical Physics*, *42*(9). https://doi.org/10.1063/1.1696408

Mukkala, A. N., Song, J. B., Lee, M., Boasie, A., Irish, J., Finelli, A., & Wei, A. C. (2021). A systematic review and meta-analysis of unplanned hospital visits and re-admissions following radical prostatectomy for prostate cancer. In *Canadian Urological Association Journal* (Vol. 15, Issue 10). https://doi.org/10.5489/cuaj.6931

NCCN. (2022). *NCCN Clinical Practice Guidelines in Oncology - Prostate Cancer 2022*. http://dx.doi.org/10.1016/B978-1-4557-2865-7.00084-9

Neal, D. E., Metcalfe, C., Donovan, J. L., Lane, J. A., Davis, M., Young, G. J., Dutton, S. J., Walsh, E. I., Martin, R. M., Peters, T. J., Turner, E. L., Mason, M., Bollina, P., Catto, J., Doherty, A., Gillatt, D., Gnanapragasam, V., Holding, P., Hughes, O., … Roberts, T. (2020). Ten-year Mortality, Disease Progression, and Treatment-related Side Effects in Men with Localised Prostate Cancer from the ProtecT Randomised Controlled Trial According to Treatment Received. *European Urology*, *77*(3). https://doi.org/10.1016/j.eururo.2019.10.030

Nyborg, W. L. (1988). Solutions of the bio-heat transfer equation. *Physics in Medicine and Biology*, *33*(7). https://doi.org/10.1088/0031-9155/33/7/002

Odéen, H., & Parker, D. L. (2019). Magnetic resonance thermometry and its biological applications – Physical principles and practical considerations. In *Progress in Nuclear Magnetic Resonance Spectroscopy* (Vol. 110). https://doi.org/10.1016/j.pnmrs.2019.01.003

Oishi, M., Gill, I. S., Ashrafi, A. N., Lin-Brande, M., Nassiri, N., Shin, T., Bove, A., Cacciamani, G. E., Ukimura, O., Bahn, D. K., & Abreu, A. L. de C. (2019). Primary Whole-gland Cryoablation for Prostate Cancer: Biochemical Failure and Clinical Recurrence at 5.6 Years of Follow-up. *European Urology*, *75*(2). https://doi.org/10.1016/j.eururo.2018.09.004

O'neill, A. G. M., Jain, S., Hounsell, A. R., & O'sullivan, J. M. (2016). Fiducial marker guided prostate radiotherapy: A review. *British Journal of Radiology*, *89*(1068), 1–18. https://doi.org/10.1259/bjr.20160296

O'Neill, A. G. M., Jain, S., Hounsell, A. R., & O'Sullivan, J. M. (2016). Fiducial marker guided prostate radiotherapy: a review. *The British Journal of Radiology*, *89*(1068), 20160296. https://doi.org/10.1259/bjr.20160296

Osman, S. O. S., Russell, E., King, R. B., Crowther, K., Jain, S., McGrath, C., Hounsell, A. R., Prise, K. M., & McGarry, C. K. (2019). Fiducial markers visibility and artefacts in prostate cancer radiotherapy multi-modality imaging. *Radiation Oncology*, *14*(1), 1–14. https://doi.org/10.1186/s13014-019-1447-1

Patel, P., & Oto, A. (2016). Magnetic Resonance Imaging of the Prostate, Including Pre- and Postinterventions. *Seminars in Interventional Radiology*, *33*(3). https://doi.org/10.1055/s-0036-1586144

Perera, M., Papa, N., Roberts, M., Williams, M., Udovicich, C., Vela, I., Christidis, D., Bolton, D., Hofman, M. S., Lawrentschuk, N., & Murphy, D. G. (2020). Gallium-68 Prostate-specific Membrane Antigen Positron Emission Tomography in Advanced Prostate Cancer—Updated Diagnostic Utility, Sensitivity, Specificity, and Distribution of Prostate-specific Membrane Antigen-avid Lesions: A Systematic Review and Meta-analysis. In *European Urology* (Vol. 77, Issue 4). https://doi.org/10.1016/j.eururo.2019.01.049

Persaud, S., Sofat, S., Lacey, N., & Datta, S. (2019). Signal voids created by prostatic urethral lift implants - a reminder in the era of multiparametric MRIs of the prostate. *International Journal of Medical Reviews and Case Reports*, *0*, 1. https://doi.org/10.5455/ijmrcr.signal-voids-prostate-mri-following-urolift

Peters, R. D., Hinks, R. S., & Henkelman, R. M. (1998). Ex vivo tissue-type independence in proton-resonance frequency shift MR thermometry. *Magnetic Resonance in Medicine*, *40*(3). https://doi.org/10.1002/mrm.1910400316

Port, J. D., & Pomper, M. G. (2000). Quantification and minimization of magnetic susceptibility artifacts on GRE images. *Journal of Computer Assisted Tomography*, *24*(6). https://doi.org/10.1097/00004728-200011000-00024

Pucar, D., Hricak, H., Shukla-Dave, A., Kuroiwa, K., Drobnjak, M., Eastham, J., Scardino, P. T., & Zelefsky, M. J. (2007). Clinically Significant Prostate Cancer Local Recurrence After Radiation Therapy Occurs at the Site of Primary Tumor: Magnetic Resonance Imaging and Step-Section Pathology Evidence. *International Journal of Radiation Oncology Biology Physics*, *69*(1). https://doi.org/10.1016/j.ijrobp.2007.03.065

Rabi, I. I., Zacharias, J. R., Millman, S., & Kusch, P. (1938). A new method of measuring nuclear magnetic moment [5]. In *Physical Review* (Vol. 53, Issue 4). https://doi.org/10.1103/PhysRev.53.318

Ramsay, C. R., Adewuyi, T. E., Gray, J., Hislop, J., Shirley, M. D., Jayakody, S., MacLennan, G., Fraser, C., MacLennan, S., Brazzelli, M., N'Dow, J., Pickard, R., Robertson, C., Rothnie, K., Rushton, S. P., Vale, L., & Lam, T. B. (2015). Ablative therapy for people with localised prostate cancer: a systematic review and economic evaluation. *Health Technology Assessment*, *19*(49), 1–490. https://doi.org/10.3310/hta19490

Reeve, B. B., Stover, A. M., Jensen, R. E., Chen, R. C., Taylor, K. L., Clauser, S. B., Collins, S. P., & Potosky, A. L. (2012). Impact of diagnosis and treatment of clinically localized prostate cancer on

health-related quality of life for older Americans: A population-based study. In *Cancer* (Vol. 118, Issue 22). https://doi.org/10.1002/cncr.27578

Resnick, M. J., Koyama, T., Fan, K.-H., Albertsen, P. C., Goodman, M., Hamilton, A. S., Hoffman, R. M., Potosky, A. L., Stanford, J. L., Stroup, A. M., van Horn, R. L., & Penson, D. F. (2013). Long-Term Functional Outcomes after Treatment for Localized Prostate Cancer. *New England Journal of Medicine*, *368*(5). https://doi.org/10.1056/nejmoa1209978

Rieke, V., & Pauly, K. B. (2008). MR thermometry. In *Journal of Magnetic Resonance Imaging* (Vol. 27, Issue 2, pp. 376–390). https://doi.org/10.1002/jmri.21265

Rivens, I., Shaw, A., Civale, J., & Morris, H. (2007). Treatment monitoring and thermometry for therapeutic focused ultrasound. *International Journal of Hyperthermia*, *23*(2). https://doi.org/10.1080/02656730701207842

Roehrborn, C. G., Barkin, J., Gange, S. N., Shore, N. D., Giddens, J. L., Bolton, D. M., Cowan, B. E., Cantwell, A. L., McVary, K. T., Te, A. E., Gholami, S. S., Moseley, W. G., Chin, P. T., Dowling, W. T., Freedman, S. J., Incze, P. F., Coffield, K. S., Herron, S., Rashid, P., & Rukstalis, D. B. (2017). Five year results of the prospective randomized controlled prostatic urethral L.I.F.T. study. *The Canadian Journal of Urology*, *24*(3), 8802–8813.

Roemeling, S., Roobol, M. J., de Vries, S. H., Wolters, T., Gosselaar, C., van Leenders, G. J. L. H., & Schröder, F. H. (2007). Active Surveillance for Prostate Cancers Detected in Three Subsequent Rounds of a Screening Trial: Characteristics, PSA Doubling Times, and Outcome. *European Urology*, *51*(5). https://doi.org/10.1016/j.eururo.2006.11.053

Ronneberger, O., Fischer, P., & Brox, T. (2015). U-Net: Convolutional Networks for Biomedical Image Segmentation. In N. Navab, J. Hornegger, W. M. Wells, & A. F. Frangi (Eds.), *Medical Image Computing and Computer-Assisted Intervention -- MICCAI 2015* (pp. 234–241). Springer International Publishing.

Rowland, I. J., Rivens, I., Chen, L., Lebozer, C. H., Collins, D. J., ter Haar, G. R., & Leach, M. O. (1997). MRI study of hepatic tumours following high intensity focused ultrasound surgery. *British Journal of Radiology*, *70*(FEB.). https://doi.org/10.1259/bjr.70.830.9135440

Sanda, M. G., Dunn, R. L., Michalski, J., Sandler, H. M., Northouse, L., Hembroff, L., Lin, X., Greenfield, T. K., Litwin, M. S., Saigal, C. S., Mahadevan, A., Klein, E., Kibel, A., Pisters, L. L., Kuban, D., Kaplan, I., Wood, D., Ciezki, J., Shah, N., & Wei, J. T. (2008). Quality of Life and Satisfaction with Outcome among Prostate-Cancer Survivors. *New England Journal of Medicine*, *358*(12). https://doi.org/10.1056/nejmoa074311

Sapareto, S. A., & Dewey, W. C. (1984). Thermal dose determination in cancer therapy. *International Journal of Radiation Oncology, Biology, Physics*, *10*(6), 787–800. https://doi.org/10.1016/0360-3016(84)90379-1

Schelb, P., Kohl, S., Radtke, J. P., Wiesenfarth, M., Kickingereder, P., Bickelhaupt, S., Kuder, T. A., Stenzinger, A., Hohenfellner, M., Schlemmer, H.-P., Maier-Hein, K. H., & Bonekamp, D. (2019). Classification of Cancer at Prostate MRI: Deep Learning versus Clinical PI-RADS Assessment. *Radiology*, *293*(3), 607–617. https://doi.org/10.1148/radiol.2019190938

Schenck, J. F. (1996). The role of magnetic susceptibility in magnetic resonance imaging: MRI magnetic compatibility of the first and second kinds. *Medical Physics*, *23*(6), 815–850. https://doi.org/10.1118/1.597854

Shah, T. T., Peters, M., Eldred-Evans, D., Miah, S., Yap, T., Faure-Walker, N. A., Hosking-Jervis, F., Thomas, B., Dudderidge, T., Hindley, R. G., McCracken, S., Greene, D., Nigam, R., Valerio, M., Minhas, S., Winkler, M., Arya, M., & Ahmed, H. U. (2019). Early-Medium-Term Outcomes of Primary Focal Cryotherapy to Treat Nonmetastatic Clinically Significant Prostate Cancer from a Prospective Multicentre Registry. *European Urology*, *76*(1). https://doi.org/10.1016/j.eururo.2018.12.030

Shahedi, M., Cool, D. W., Romagnoli, C., Bauman, G. S., Bastian-Jordan, M., Gibson, E., Rodrigues, G., Ahmad, B., Lock, M., Fenster, A., & Ward, A. D. (2014). Spatially varying accuracy and reproducibility of prostate segmentation in magnetic resonance images using manual and semiautomated methods. *Medical Physics*, *41*(11), 1–15. https://doi.org/10.1118/1.4899182

Shellock, F. G., & Morisoli, S. M. (1994). Ex vivo evaluation of ferromagnetism, heating, and artifacts produced by heart valve prostheses exposed to a 1.5-T MR system. *Journal of Magnetic Resonance Imaging*, *4*(5). https://doi.org/10.1002/jmri.1880040521

Shellock, F. G., & Shellock, V. J. (1996). Vascular access ports and catheters: Ex vivo testing of ferromagnetism, heating, and artifacts associated with MR imaging. *Magnetic Resonance Imaging*, *14*(4). https://doi.org/10.1016/0730-725X(95)02114-9

Shen, G., Deng, H., Hu, S., & Jia, Z. (2014). Comparison of choline-PET/CT, MRI, SPECT, and bone scintigraphy in the diagnosis of bone metastases in patients with prostate cancer: a meta-analysis. In *Skeletal Radiology* (Vol. 43, Issue 11). https://doi.org/10.1007/s00256-014-1903-9

Siddiqui, K. M., Billia, M., Al-Zahrani, A., Williams, A., Goodman, C., Arifin, A., Violette, P., Bauman, G., & Chin, J. L. (2016). Long-Term Oncologic Outcomes of Salvage Cryoablation for Radio-Recurrent Prostate Cancer. *The Journal of Urology*, *196*(4), 1105–1111. https://doi.org/10.1016/j.juro.2016.04.080

Silver, D. A., Pellicer, I., Fair, W. R., Heston, W. D. W., & Cordon-Cardo, C. (1997). Prostate-specific membrane antigen expression in normal and malignant human tissues. *Clinical Cancer Research*, *3*(1).

Soloway, M. S., Soloway, C. T., Eldefrawy, A., Acosta, K., Kava, B., & Manoharan, M. (2010). Careful selection and close monitoring of low-risk prostate cancer patients on active surveillance minimizes the need for treatment. *European Urology*, *58*(6). https://doi.org/10.1016/j.eururo.2010.08.027

Stafford, R. J., Price, R. E., Diederich, C. J., Kangasniemi, M., Olsson, L. E., & Hazle, J. D. (2004). Interleaved echo-planar imaging for fast multiplanar magnetic resonance temperature imaging of ultrasound thermal ablation therapy. *Journal of Magnetic Resonance Imaging*, *20*(4). https://doi.org/10.1002/jmri.20157

Stamey, T. A., Yang, N., Hay, A. R., McNeal, J. E., Freiha, F. S., & Redwine, E. (1987). Prostate-Specific Antigen as a Serum Marker for Adenocarcinoma of the Prostate. *New England Journal of Medicine*, *317*(15). https://doi.org/10.1056/nejm198710083171501

Staruch, R. M., Nofiele, J., Walker, J., Bing, C., Madhuranthakam, A. J., Bailey, A., Kim, Y. S., Chhabra, A., Burns, D., & Chopra, R. (2017). Assessment of acute thermal damage volumes in muscle using magnetization-prepared 3D T2-weighted imaging following MRI-guided high-intensity focused ultrasound therapy. *Journal of Magnetic Resonance Imaging*, *46*(2), 354–364. https://doi.org/10.1002/jmri.25605

Sugimura, K., Carrington, B. M., Quivey, J. M., & Hricak, H. (1990). Postirradiation changes in the pelvis: Assessment with MR imaging. *Radiology*, *175*(3). https://doi.org/10.1148/radiology.175.3.2343132

Suomi, V., Komar, G., Sainio, T., Joronen, K., Perheentupa, A., & Blanco Sequeiros, R. (2019). Comprehensive feature selection for classifying the treatment outcome of high-intensity ultrasound therapy in uterine fibroids. *Scientific Reports*, *9*(1). https://doi.org/10.1038/s41598-019-47484-y

Suomi, V., Treeby, B., Jaros, J., Makela, P., Anttinen, M., Saunavaara, J., Sainio, T., Kiviniemi, A., & Blanco, R. (2018). Transurethral ultrasound therapy of the prostate in the presence of calcifications: A simulation study. *Medical Physics*, *45*(11), 4793–4805. https://doi.org/10.1002/mp.13183

Sweat, S. D., Pacelli, A., Murphy, G. P., & Bostwick, D. G. (1998). Prostate-specific membrane antigen expression is greatest in prostate adenocarcinoma and lymph node metastases. *Urology*, *52*(4). https://doi.org/10.1016/S0090-4295(98)00278-7

Taber, K. H., Herrick, R. C., Weathers, S. W., Kumar, A. J., Schomer, D. F., & Hayman, L. A. (1998). Pitfalls and Artifacts Encountered in Clinical MR Imaging of the Spine. *Radiographics*, *18*(6). https://doi.org/10.1148/radiographics.18.6.9821197

Takenaka, A., Murakami, G., Matsubara, A., Han, S. H., & Fujisawa, M. (2005). Variation in course of cavernous nerve with special reference to details of topographic relationships near prostatic apex: Histologic study using male cadavers. *Urology*, *65*(1). https://doi.org/10.1016/j.urology.2004.08.028

Taylor, K. L., Luta, G., Hoffman, R. M., Davis, K. M., Lobo, T., Zhou, Y., Leimpeter, A., Shan, J., Jensen, R. E., Aaronson, D. S., & van den Eeden, S. K. (2018). Quality of life among men with

low-risk prostate cancer during the first year following diagnosis: The PREPARE prospective cohort study. *Translational Behavioral Medicine*, *8*(2). https://doi.org/10.1093/tbm/ibx005

Tosoian, J. J., Mamawala, M., Epstein, J. I., Landis, P., Wolf, S., Trock, B. J., & Carter, H. B. (2015). Intermediate and longer-term outcomes from a prospective active-surveillance program for favorable-risk prostate cancer. *Journal of Clinical Oncology*, *33*(30). https://doi.org/10.1200/JCO.2015.62.5764

Tran, H., Kwok, J., Pickles, T., Tyldesley, S., & Black, P. C. (2014). Underutilization of local salvage therapy after radiation therapy for prostate cancer. *Urologic Oncology: Seminars and Original Investigations*, *32*(5). https://doi.org/10.1016/j.urolonc.2013.12.014

Turkbey, B., Rosenkrantz, A. B., Haider, M. A., Padhani, A. R., Villeirs, G., Macura, K. J., Tempany, C. M., Choyke, P. L., Cornud, F., Margolis, D. J., Thoeny, H. C., Verma, S., Barentsz, J., & Weinreb, J. C. (2019). Prostate Imaging Reporting and Data System Version 2.1: 2019 Update of Prostate Imaging Reporting and Data System Version 2. In *European Urology* (Vol. 76, Issue 3). https://doi.org/10.1016/j.eururo.2019.02.033

Valerio, M., Cerantola, Y., Eggener, S. E., Lepor, H., Polascik, T. J., Villers, A., & Emberton, M. (2017). New and Established Technology in Focal Ablation of the Prostate: A Systematic Review [figure presented]. In *European Urology* (Vol. 71, Issue 1). https://doi.org/10.1016/j.eururo.2016.08.044

Valle, L. F., Lehrer, E. J., Markovic, D., Elashoff, D., Levin-Epstein, R., Karnes, R. J., Reiter, R. E., Rettig, M., Calais, J., Nickols, N. G., Dess, R. T., Spratt, D. E., Steinberg, M. L., Nguyen, P. L., Davis, B. J., Zaorsky, N. G., & Kishan, A. U. (2021). A Systematic Review and Meta-analysis of Local Salvage Therapies After Radiotherapy for Prostate Cancer (MASTER). *European Urology*, *80*(3), 280–292. https://doi.org/10.1016/j.eururo.2020.11.010

van As, N. J., Norman, A. R., Thomas, K., Khoo, V. S., Thompson, A., Huddart, R. A., Horwich, A., Dearnaley, D. P., & Parker, C. C. (2008). Predicting the Probability of Deferred Radical Treatment for Localised Prostate Cancer Managed by Active Surveillance. *European Urology*, *54*(6). https://doi.org/10.1016/j.eururo.2008.02.039

Vargas, H. A., Wassberg, C., Akin, O., & Hricak, H. (2012). MR imaging of treated prostate cancer. In *Radiology* (Vol. 262, Issue 1). https://doi.org/10.1148/radiol.11101996

Venkatesan, A. M., Partanen, A., Pulanic, T. K., Dreher, M. R., Fischer, J., Zurawin, R. K., Muthupillai, R., Sokka, S., Nieminen, H. J., Sinaii, N., Merino, M., Wood, B. J., & Stratton, P. (2012). Magnetic resonance imaging-guided volumetric ablation of symptomatic leiomyomata: Correlation of imaging with histology. *Journal of Vascular and Interventional Radiology*, *23*(6). https://doi.org/10.1016/j.jvir.2012.02.015

Viitala, A., Anttinen, M., Wright, C., Virtanen, I., Mäkelä, P., Hovinen, T., Sainio, T., Saunavaara, J., Taimen, P., Blanco Sequeiros, R., & Boström, P. J. (2021). Magnetic resonance imaging-guided transurethral ultrasound ablation for benign prostatic hyperplasia: 12-month clinical outcomes of a phase I study. *BJU International*. https://doi.org/10.1111/bju.15523

Walsh, P. C. (1997). Immediate versus deferred treatment for advanced prostatic cancer: initial results of the Medical Research Council trial. The Medical Research Council Prostate Cancer Working Party Investigators Group. *The Journal of Urology*, *158*(4).

WALSH, P. C., & MOSTWIN, J. L. (1984). Radical Prostatectomy and Cystoprostatectomy with Preservation of Potency. Results Using a New Nerve-sparing Technique. *British Journal of Urology*, *56*(6). https://doi.org/10.1111/j.1464-410X.1984.tb06149.x

Walz, J., Epstein, J. I., Ganzer, R., Graefen, M., Guazzoni, G., Kaouk, J., Menon, M., Mottrie, A., Myers, R. P., Patel, V., Tewari, A., Villers, A., & Artibani, W. (2016). A Critical Analysis of the Current Knowledge of Surgical Anatomy of the Prostate Related to Optimisation of Cancer Control and Preservation of Continence and Erection in Candidates for Radical Prostatectomy: An Update. In *European Urology* (Vol. 70, Issue 2). https://doi.org/10.1016/j.eururo.2016.01.026

Weidensteiner, C., Quesson, B., Caire-Gana, B., Kerioui, N., Rullier, A., Trillaud, H., & Moonen, C. T. W. (2003). Real-time MR temperature mapping of rabbit liver in vivo during thermal ablation. *Magnetic Resonance in Medicine*, *50*(2). https://doi.org/10.1002/mrm.10521

Weishaupt, D., Köchli, V., & Marincek, B. (2006). *How Does MRI Work?: An Introduction to the Physics and Function of Magnetic Resonance Imaging*. https://doi.org/10.1007/978-3-540-37845-7

Wijlemans, J. W., Deckers, R., van den Bosch, M. A. A. J., Seinstra, B. A., van Stralen, M., van Diest, P. J., Moonen, C. T. W., & Bartels, L. W. (2013). Evolution of the ablation region after magnetic resonance-guided high-intensity focused ultrasound ablation in a Vx2 tumor model. *Investigative Radiology*, *48*(6). https://doi.org/10.1097/RLI.0b013e3182820257

Williams, S. B., & Hu, J. C. (2013). Salvage robotic assisted laparoscopic radical prostatectomy: Indications and outcomes. *World Journal of Urology*, *31*(3). https://doi.org/10.1007/s00345-010-0619-2

Wilt, T. J., Jones, K. M., Barry, M. J., Andriole, G. L., Culkin, D., Wheeler, T., Aronson, W. J., & Brawer, M. K. (2017). Follow-up of prostatectomy versus observation for early prostate cancer. *New England Journal of Medicine*, *377*(2), 132–142.

Winter, L., Oberacker, E., Paul, K., Ji, Y., Oezerdem, C., Ghadjar, P., Thieme, A., Budach, V., Wust, P., & Niendorf, T. (2016). Magnetic resonance thermometry: Methodology, pitfalls and practical solutions. *International Journal of Hyperthermia*, *32*(1), 63–75. https://doi.org/10.3109/02656736.2015.1108462

Wise, A. M., Stamey, T. A., McNeal, J. E., & Clayton, J. L. (2002). Morphologic and clinical significance of multifocal prostate cancers in radical prostatectomy specimens. *Urology*, *60*(2). https://doi.org/10.1016/S0090-4295(02)01728-4

Zhu, M., Sun, Z., & Ng, C. K. (2017). Image-guided thermal ablation with MR-based thermometry. *Quantitative Imaging in Medicine and Surgery*, *7*(3), 356–368. https://doi.org/10.21037/qims.2017.06.06

Zhu, Q., Du, B., Turkbey, B., Choyke, P. L., & Yan, P. (2017). Deeply-supervised CNN for prostate segmentation. *Proceedings of the International Joint Conference on Neural Networks*, *2017-May*, 178–184. https://doi.org/10.1109/IJCNN.2017.7965852

TURUN
YLIOPISTO
UNIVERSITY
OF TURKU

Painosalama, Turku, Finland 2023

ISBN 978-951-29-9182-2 (PRINT)
ISBN 978-951-29-9183-9 (PDF)
ISSN 0355-9483 (Print)
ISSN 2343-3213 (Online)